HYPED

HYPERLOOP EDINBURGH

EHW 2024 FINAL RESEARCH PROPOSAL

Enhancing Hyperloop Sustainability Through Optimal Pod Design and Vacuum Maintenance

THE UNIVERSITY of EDINBURGH

Enhancing Hyperloop Sustainability Through Optimal Pod Design and Vacuum Maintenance

C. Looney, B.A. Ganesh, A. Leelapanang, L. Armstrong, M.W.B.A. Islah, M.H. Charan, K. Bhatnagar, I.Rosli, S.H. Kuruganti, P. Modi, S. Desai

HYPED Research Team
9th June 2024

Contents

List of Figures

List of Tables

Abstract

Hyperloop transportation is touted as a sustainable solution to the growing demand for rapid transportation. To improve the sustainability, the system must be energetically optimised. Hyperloop transportation utilizes vacuum tubes to minimize the drag acting on a pod. A stronger vacuum implies less drag will act on the pod however, the vacuum itself will require more input to maintain. This implies a trade-off exists between the energy demands of vacuum maintenance and drag loss. Therefore, there exists an optimal tube pressure in which overall energy consumption is minimised. In this study, three different vacuum pumps are investigated regarding their suitability in a hyperloop: cryopumps, turbomolecular pumps, and dry screw pumps. It was found that the turbomolecular pump, back with a dry screw pump, will be the most effective for the hyperloop. The effects of implementing a compressor on the pod, specifically the drag reduction, are investigated. These results are then combined to estimate the optimal tube range to be between 500 and 1000 Pa.

To effectively implement the compressor, and utilize the aerodynamics of the pod to benefit the system, a complete pod design was created. It was determined that a nose-and-tail down pod configuration positively impacted the lift on the pod and is therefore the recommended configuration. Aluminium alloy, polyetheretherketone, and polyaryletherketone were investigated as potential pod materials. polyaryletherketone demonstrated favourable characteristics and was chosen as the optimal pod material of the three. Finally, it was determined that the optimal length of the pod should be determined on a case-by-case basis as it is dependent on the length of travel.

Word count: 15151

Location of Publication: https://www.hyp-ed.com/research

1 Introduction

The hyperloop was initially proposed as a sustainable solution to the ever-growing demand for rapid transportation due to its minimal operating energy demand [18]. The near-vacuum environment of a hyperloop system effectively removes friction drag on the pod; however, due to the high-speed nature of the system, intense pressure gradients and shockwaves can form around the pod, greatly increasing pressure drag acting on the system [24]. The implementation of an axial air compressor into the pod is theorised to be the most popular solution to this issue [7].

At the time of this study, no comprehensive analysis of the energy efficiency of the hyperloop has been conducted. While numerous studies have been conducted on reducing pressure drag in the hyperloop, no studies have synthesised the drag reduction on the pod system and the energy needed to maintain the vacuum [7, 8, 25]. Furthermore, the studies that have simulated a compressor implementation have not created a complete pod design with considerations of passenger accessibility, aerodynamic shape of the pod, and the pod construction material.

The primary objective of this paper is to minimise energy loss due to system inefficiency and increase system sustainability through the consideration of pod design and vacuum pumps. The efficiency of the axial compressor will be thoroughly investigated, determining the precise effects the compressor has on the drag acting on the system. The main effect to be investigated is the reduction of the pressure differential between the front and rear of the pod. Additionally, it will be investigated whether the egressing compressed air is more effectively used as a source of lift or propulsion for the pod. The central conclusion to be determined is how much energy the pod loses due to drag after the implementation of the compressor.

This study aims to produce a model for the hyperloop pod, designed such that the compressor can be effectively used. Further details on the pod design will be investigated including the effect of the head shape on pod drag, not including the compressor, and the effect of the tail shape on efficiency. Primarily, the tail will be investigated as a source of lift due to airflow over the pod.

For completeness, an investigation of the pod interior design will be conducted to ensure the practicality of the design. The interior will be designed in a way that maximises efficiency through considerations such as passenger numbers and a modular system to accommodate passenger and cargo transportation. The materials used to construct the exterior of the pod will be researched to reduce the long-term environmental impact of the hyperloop. The materials to be investigated include aluminium alloy, polyetheretherketone (PEEK), and polyaryletherketone (PAEK). These materials were chosen due to their importance in the sustainable aerospace field.

Finally, three vacuum pumps will be investigated through a literature review for their feasibility in operating in the hyperloop system. The pumps, dry-screw, turbomolecular, and cryopumps, were chosen due to their ability to reach extreme vacuum strengths or low maintenance. The pumps are evaluated based on their energy efficiency in maintaining a given vacuum, the maintenance required, and any external characteristics specific to the pump that could affect its suitability. Finally, with an assumed leakage rate, the energy efficiency of the pump in maintaining a variable vacuum strength will be determined.

As stated, the energy loss for a pod travelling in a given vacuum due to pressure drag will be determined after analysing the effects of a compressor implemented on the pod. Secondly, for a recommended vacuum pump, the energy required to maintain a certain vacuum strength against an assumed leakage rate will be determined. These results will be synthesised to provide an estimate for the optimal vacuum strength of the hyperloop system. This is due to vacuum maintenance energy being inversely proportional to the pressure drag on the pod, implying a minimum exists for total operating energy.

2 Vacuum Pumps

In a hyperloop system, vacuum pumps are responsible for the creation and maintenance of a low-pressure environment within the tube. A near-vacuum tube will significantly reduce the drag acting on the pod and allow it to travel at a more ideal speed. The vacuum pump to be used should be selected based on several criteria including the ability to reach extreme vacuum strengths efficiently, minimal maintenance, and the overall energy efficiency of the pump.

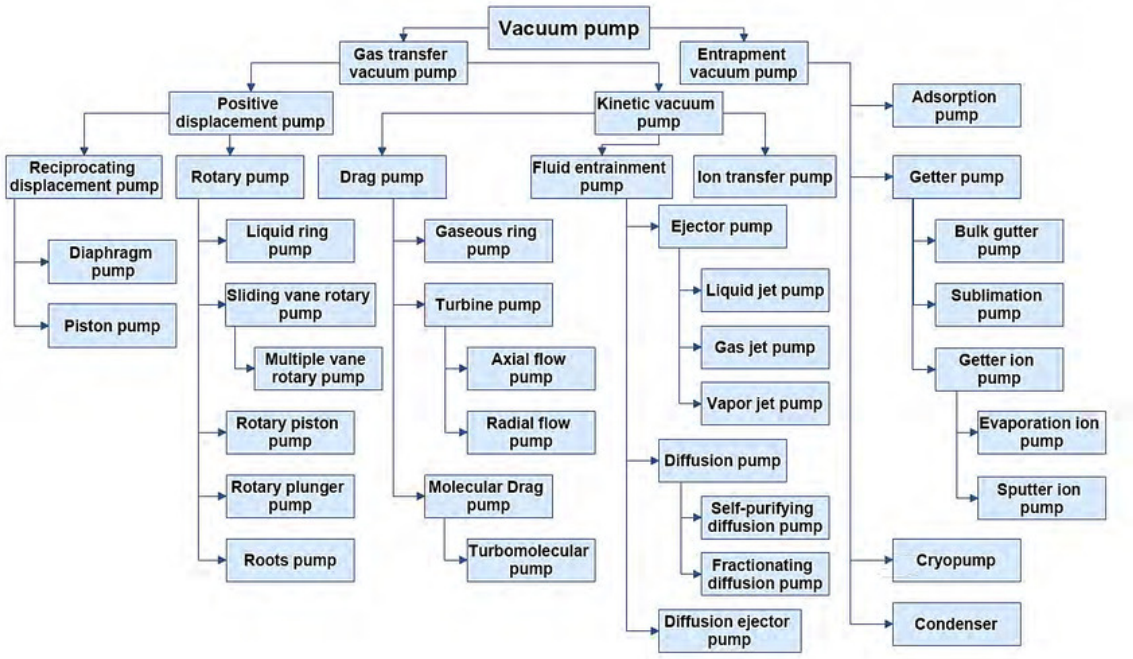

Figure 1: Overview of Vacuum Pump Classifications [1]

In this paper, three vacuum pumps will be investigated. The first, a turbomolecular pump, is a drag pump. Drag pumps utilise the drag of gas molecules against the rotating surface of the pump to create a vacuum. These pumps can reach high vacuum strengths with relatively minimal maintenance. The second pump, a cryopump, is an entrapment pump. Entrapment pumps use chemical reactions to trap and remove the gas molecules. These pumps are known for their ability to create high and ultra-high vacuums. Finally, a dry screw pump is investigated. Dry vacuum pumps are known for requiring little maintenance and their lack of hydrocarbons.

2.1 Turbomolecular Vacuum Pump

2.1.1 Mechanism

Turbomolecular vacuum pumps, or TMPs, are an industry standard when strong vacuums are required. The TMPs operate like their predecessor, the molecular drag pumps which were developed in the early 20th century. The principal physics behind these vacuum pumps is the same: pressure gradients can be produced in gasses by the imparted directional velocities from collisions. The particles will enter the opening of the pumps, where they will be impacted by an angled rotor blade. These blades are typically set at 45° from the horizontal, which results in optimal gas glow. As a result of the impacts, the gas is redirected downwards, giving the gas downward momentum as it spirals down the mechanism. Stators are routinely placed between the rotors to prevent the backflow of gasses [26]. These stators prevent the backflow of gasses, as any particle which is flowing backwards will likely be redirected back downwards. After the particles have flowed through the mechanisms of the pump, they are sent through a channel

and exit the mechanism, and a vacuum is achieved. TMPs are usually able to achieve a vacuum strength of roughly $1.8 \times 10^{-7}\, Pa$, a far greater vacuum strength than most of the TMPs contemporaries [2].

TMPs generally consist of three main types: magnetically suspended, partial magnetic suspension (also referred to as hybrids), and mechanical rolling element TMPs. These variations are all centred around the issue of rotation of the blades. In order to achieve the high vacuum strength typical with TMPs, the rotors need to spin anywhere from 24,000 to 90,000 rpm, mandating a near absence of friction on the rotors. Magnetically suspended TMPs use magnets to suspend the rotors, such that they do not experience any friction from surface collisions as shown in figure 2. These result in ultra-strong and clean vacuums, as there is no possibility of contamination from outside particles, or from pieces of the bearings breaking off, becoming contaminants themselves. Mechanical rolling TMPs use oil-lubricated ball bearings in order to reduce friction. This is not as efficient as magnetically suspended pumps; however, it is much less expensive and has the potential to cause contaminates as the lubricant can leak into other areas of the TMP [27]. Hybrid TMPs use a combination of both methods to achieve a lack of friction, as such it is a middle ground between the three types.

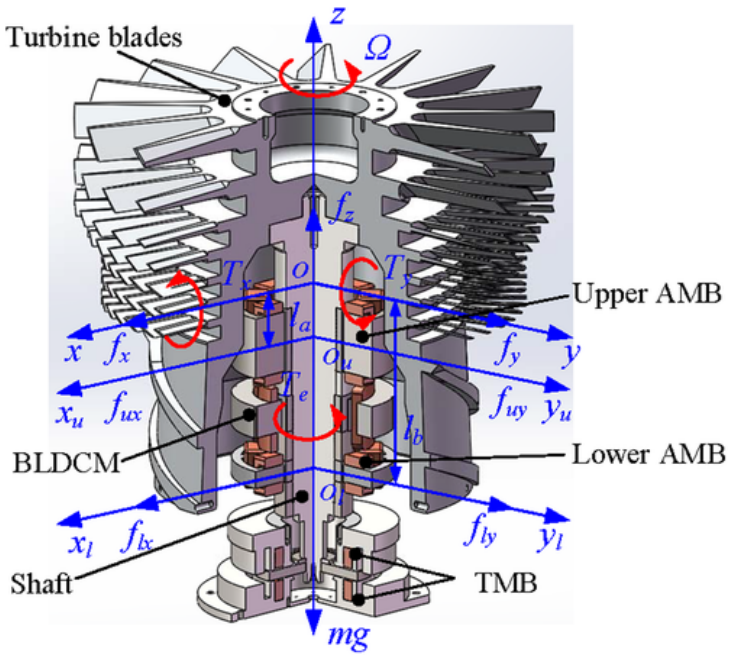

Figure 2: Turbomolecular Pump Design [2]

2.1.2 Issues and Potential Modifications

Without the assistance of a heat exchanger or some other form of cooling device, the high-energy rotations cause an immense buildup of heat within the mechanism. This impedes the creation of a vacuum in a number of ways. Not only will the rotor blades themselves expand, but depending on the type of TMP (magnetic, non-magnetic, etc.) the lubricant will become viscous, increasing friction and adding heat into the system [28].

Each type of TMP provides unique solutions to the issues prevalent within the system. One of the most pressing issues is the formation of magnetic eddy currents, shown in figure 3, due to the rapidly rotating magnetic blades of the pump. These eddy currents cause the rotor blades to heat up, slowing down rotation. These magnetic fields can either form parallel or orthogonal (with respect to the rotating axis) to the TMPs; it is important to note that while the orthogonal fields have a significant impact on driving power and rotor temperature, their counterparts in the parallel fields have relatively low impact [29]. This relationship is explained as the spinning rotors have near-perfect symmetry about the axis of rotation; thus there is no magnetic flux when the field is parallel. The orthogonal fields' impact is most noticeable during acceleration and deceleration of the rotor blades, during this time the eddy current loss is proportional to H^2 where H is the magnetic field strength. These eddy currents are also

responsible for an estimated temperature increase of up to $5°C$ [29]. As a TMP's only source of cooling is through the radiation of heat (i.e. there is no active cooling system), this increase in temperature is detrimental.

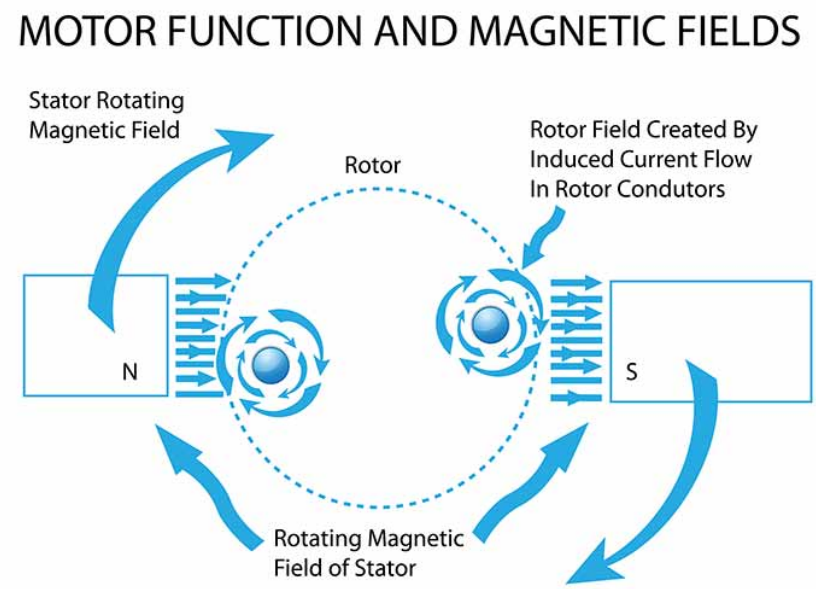

Figure 3: Turbomolecular Pump Magnetic Eddy Currents [3]

There are, however, several ways to get around these issues. One promising idea is the use of a ceramic rotor to circumvent the issue of eddy currents [30]. While there remain some unanswered questions about these types of TMPs, especially pertaining to whether or not they will be able to create the strong vacuum fields synonymous with TMPs, the evidence so far, however, is promising [30]. Not only was there no response to any outside magnetic fields with these blades, but an *rpm* of 30,000 (which is within the standard range of 24,000 - 90,000 *rpm*) was achieved (although it should be noted that there is a 10% probability of a rupture occurring at 38500 *rpm*) [30]. This is an incredibly convenient solution as ceramic is not only magnetically sensitive but also oil-free, contributing to an overall cleaner vacuum. Additionally, new research is being done into other materials for the rotors, with the hope of raising the heat resistance of TMPs. One study conducted with pre-stressed Aluminum 7050 blades showed a temperature reduction of $33°C$, demonstrating the opportunity for further optimization of the TMP [31].

Heat is not the only way that the TMPs can become damaged though, as they are particularly susceptible to vibrations and particulate. Particles entering the system will be rapidly accelerated while colliding with the rotor blades, resulting in serious damage to the components. Vibrations can cause damage in two ways. If there is a rotor unbalance (misalignment between the centre of rotation and centre of mass) causing vibrations, then this is normally minor and can be resolved by dynamic balancing, which is the combination of masses in two separate rotor zones although, this will become a larger issue if not addressed quickly [28]. Larger vibrations indicate an issue with the bearings, primarily being the presence of wear particles in the system, which again will be accelerated to great speeds causing potential damage.

Despite their incredible vacuum strength, TMPs do not draw an overwhelming amount of power. For an average turbomolecular pump, the max power consumption is around 240 W [32]. This is notably less than the TMPs competitors. Additionally, the pumping speeds of such a TMP can range anywhere from $290 - 440\, l\, s^{-1}$, depending on both the specific type of TMP, as well as the mass of the molecules being pumped [32]. It should be noted for atmospheric conditions, where air is assumed to be primarily nitrogen, the pumping speed will either be $290\, l\, s^{-1}$ or $430\, l\, s^{-1}$ [32]. Top-of-the-line TMPs have achieved pumping speeds up to $3000\, l\, s^{-1}$ [33].

2.1.3 Necessity of Forepump for Turbomolecular Pump

TMPs are at core, kinetic and molecular drag pumps. As such, they depend on the Monte Carlo principle in order to create a vacuum. This however has an issue, for the Monte Carlo principle to take effect, the pump has to be rid of atmospheric pressure. While TMPs are one of the strongest commercially available vacuum pumps, they are unable to create a vacuum unaided, as TMPs cannot expel any gasses in the vacuum chamber against atmospheric pressure [26]. Additionally, it takes quite a long time (anywhere from 5 to 15 minutes depending on the type of TMP) for the rotor blades to reach their top speed, and consequently, the peak vacuum will not be achieved until the top speed is achieved. To correct this issue, a forepump is often used in conjunction with the TMP. The forepump's purpose is to get an initial, weaker vacuum, to allow for the second, stronger vacuum to work efficiently.

2.2 Cryopump

A cryopump is a vacuum pump which entraps gas through condensation or adsorption on its internal surfaces that are cooled to temperatures below 120 K. It is categorized under entrapment or capture vacuum pumps [4]. Cryopumps are capable of achieving ultra-high vacuum (UHV) range (10^{-6} to 10^{-10} Pa) due to their ability to pump all, including noble gas at low enough temperatures [4]. They are often used in space simulations, nuclear fusion devices, magnetic resonance imaging (MRI), as well as semiconductor and coating industries [4, 34, 35].

Cryopumping effects can be divided into two stages; cryocondesation and cryosorption, which are further discussed in the upcoming sections.

2.2.1 Mechanism

Cryocondensation

To effectively capture and condense the gases, a cryopump must be cooled to a temperature where the corresponding saturation pressure is less than or equal to the desired vacuum pressure [4]. As demonstrated in Figure 4, the saturation curve of the gases will become identical to the respective sublimation curves.

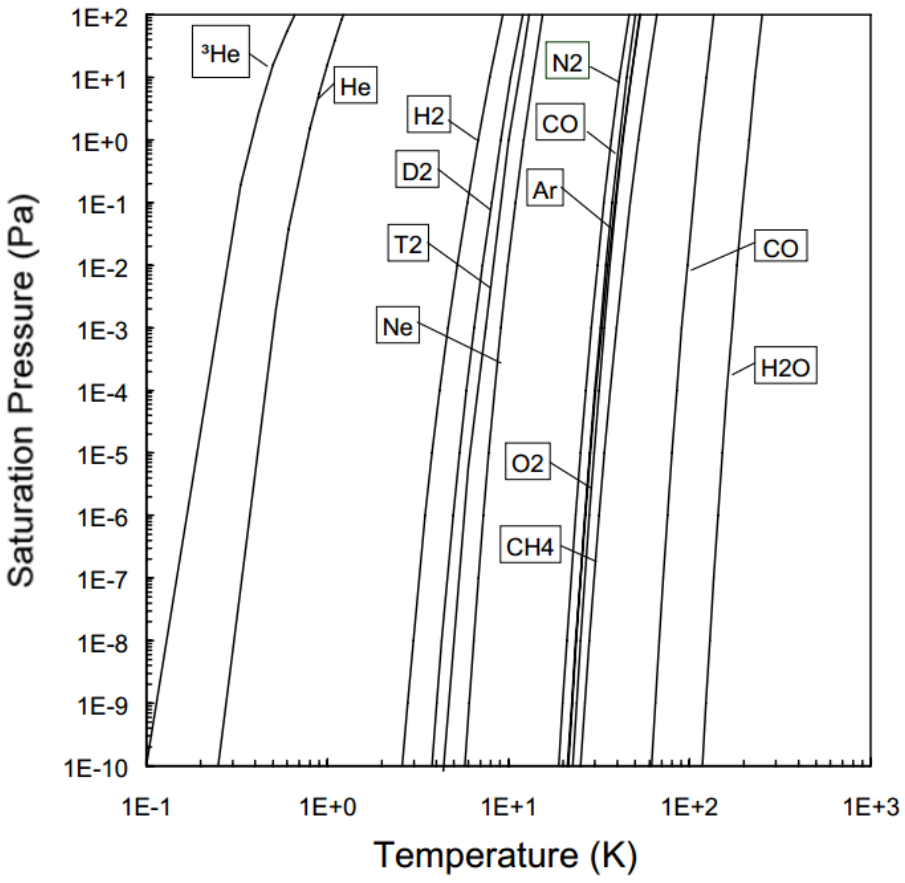

Figure 4: Saturation curves of common gases [4]

As illustrated in Figure 4, a temperature below 100 K is sufficient to condense water vapour and hydrocarbon, while reaching under 20 K is needed to condense air components such as nitrogen and oxygen. However, neon, hydrogen isotopes and helium require the lowest temperature to condense, around 4 K.

Cryosorption

Since neon, hydrogen and helium are very difficult to condense, an additional approach is applied by cryopumps: cryosorption, which is the physical adsorption process under vacuum conditions and low temperatures [4]. This process is defined as the attachment of gas particles on a low-temperature surface by weak intermolecular forces after losing their incident kinetic energy. Cryosorption is indispensable in cryopumps because the equilibrium pressure of adsorbed gas particles is considerably lower than the corresponding saturation pressure for cryocondensation, allowing the particles to be retained at a higher temperature. As a result, most cryopumps come equipped with a layer of porous materials with high sorption capacity on their internal surfaces to aid in the process. Numerous materials have been used the cryosorbent, including zeolite, condensed gas, and carbon fibers, but studies have agreed that activated charcoals, especially coconut-shell-based materials, have the best pumping attributes [4,36].

Regeneration

There is a hurdle that any cryopumps will face; the accumulation of gas and impurities on its surface that exceeds its capacity limit. In order for cryopumps to continue functioning effectively, regeneration must be regularly done to release the trapped gas. Regeneration involves heating up the cryopanels back to room temperature or more, either by turning off the refrigeration unit and allowing the pump to naturally warm up, or with the aid of additional methods. Generally, these methods are automatically activated by a system that monitors the pump's performance, and include the injection of inert purge gas, the use of built-in heaters, infrared, glow discharge, microwave and synchrotron radiation heating [4]. Once it reaches an equilibrium temperature with the environment, a valve is opened to liberate the retained gas into the atmosphere. Regeneration normally lasts for tens of minutes [4].

Designs

There have been several cryopump designs since its conception, but four main components are present in all of them; the vacuum chamber, baffles, radiation shield and cryopanels [36]. The key differentiation between cryopumps designs is the method employed to cool the cryopanels.

Early cryopumps make use of liquid cryogens such as liquid nitrogen (LN), liquid neon, liquid hydrogen, and liquid helium (LHe) to cool down. This is known as a bath cryopump [4]. The three liquid cryogens create three stages inside the cryopumps with different temperatures which correspond to the temperatures needed to condense water and hydrocarbons (100 K), gas components (80 K) and hydrogen and helium cryosorption (4 K). Figure 5 demonstrates a typical set-up of a bath cryopump.

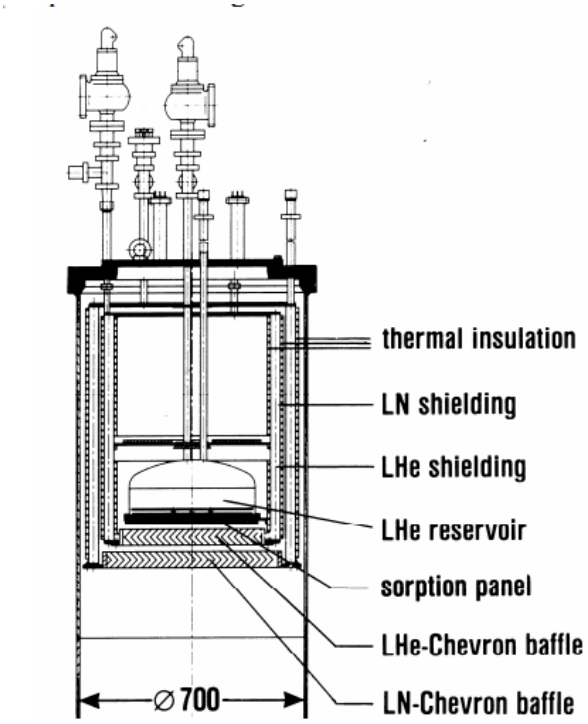

Figure 5: Typical set-up of a bath cryopump in three-stage configuration. [4]

Nowadays, practically every commercially available cryopump makes use of closed-loop mechanical refrigerators, using helium as a working fluid [4, 37]. Specifically, the Gifford-McMahon cryocooler. This is because the use of liquid cryogens carries a great risk if an error were to occur, as well as requiring high capital and operational costs [4]. A refrigerator-cooled cryopump also surpassed bath cryopumps by requiring limited care and being able to operate for long periods [34]. A typical set-up is shown in Figure 6 below.

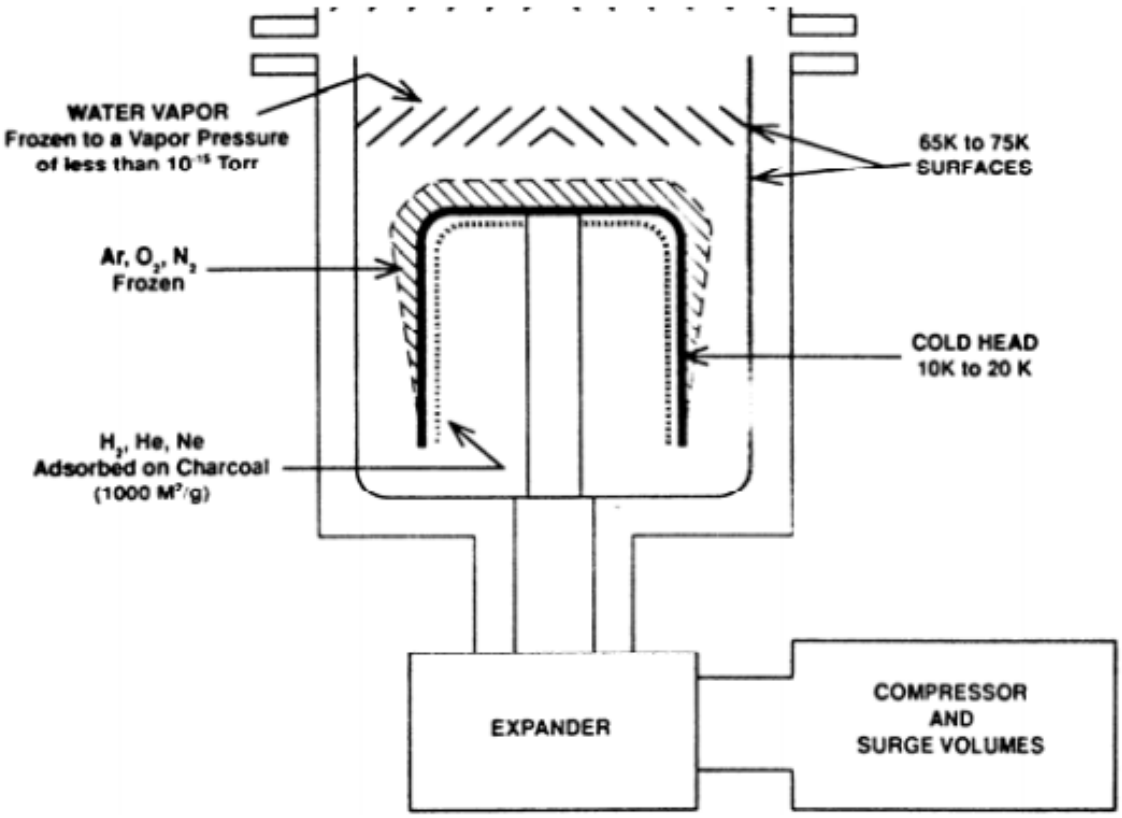

Figure 6: Typical setup of a two-stage refrigerator-cooled cryopump [4]

The compressor and the expander are connected via a flexible hose and the gaseous helium is constantly flowing between them. G-M-refrigerator-cooled cryopumps are usually composed of two stages, one which operates between 50 to 75 K to cool the structures that provide the radiation shielding and the baffles across the inlet of the pump, and another which operates at 10 K or lower, to cool the inner cryopanels [4, 34, 35]. Sorbent materials are added in the second stage for cryosorption [4, 36].

A setback that comes with refrigerator-cooled cryopumps, however, is its small scale due to the limited refrigeration power [4]. The largest commercially available cryopumps typically come with a diameter between 20 to 25 inches [20,21]. Furthermore, it has to rely primarily on cryosorption to pump helium and hydrogen due to its inability to reach a temperature of 4 K, although specially-designed cryopumps were able to overcome this problem and eliminate the need for sorption materials [34, 35]. Nevertheless, while it is possible to rely solely on cryocondensation, cryosorbent materials with high internal surfaces provide a great capacity for adsorption due to the dependence on surface area by cryosorption pumping [4].

2.2.2 Pumping Speed and Power Demand

There have been a multitude of cryopumps developed by numerous industries, all with varying parameters. Figure **??** listed several averaged parameters of cryopumps from the catalogue of different manufacturers in 2007.

Table 1: Listed performance data (average taken from the catalogue of different manufacturers) for a typical 3000 $l\,s^{-1}$ class two-stage GM cryopump [4]

Parameter	Value
Pumping Speed ($l\,s^{-1}$)	
Water	9000 - 10500
Air	3000 3250
Hydrogen	4500 - 5200
Argon	2500 - 2700
Helium	1500 - 2300
Maximum throughput ($Pa\,m^3\,s^{-1}$)	
Argon	1.0 - 2.5
Hydrogen	1.2
Pumping Capacity ($Pa\,m^3$)	
Argon	$1.5 \times 10^5 - 3 \times 10^5$
Hydrogen	1500 - 5000
Helium	10 - 100
Ultimate Pressure (N_2 equivalent)(Pa)	$10^{-9} - 10^{-10}$
Cool-down time (h)	1.5 - 2.5
Crossover ($Pa\,m^3$)	35 - 50
Weight (kg)	30 - 50

According to the dataset, the pumping speed of air ranges between 3000 to 3250 $l\,s^{-1}$. Yet, a large capacity cryopump developed by Korea Institute of Machinery and Materials (KIMM) has reached an air pumping speed of over 10,000 $l\,s^{-1}$ [20], as shown in Figure **??**. This demonstrates that higher pumping speed for air is achievable.

Table 2: Specifications of the GM cryocooler and cryopump developed by KIMM [20]

Cryopump	Opening size		20-inch(DN500)
	Pumping speed		$10{,}000 l\,s^{-1}$
	Ultimate pressure		$10^{-}9\,mbar - class$
	Cooldown time		$< 160\,min$
GM Cryocooler	Cooling capacity	First stage	$80W$ at $80K$
		Second stage	$8W$ at $20K$
	Electric power consumption		$< 7.5kW$
	Cooldown time		$< 50min$

In terms of power demand, a series of cryopumps with a diameter of 22 inches by Ulvac Cryogenics Inc. has undergone a decrease in power consumption over time as shown in Figure **??**; effectively lowering the power consumption to 4.2 kW [21]. Their air pumping speed also reaches the same level as the one developed by KIMM [21].

Table 3: Specifications of 22-inch cryopump series [21]

		First Generation	Second	Generation	Third Generation
Cryopump	Model	U22H	U22B	U22BL	U22BL
	Quantity	1	1	1	2
Refrigerator	Model	RM50T	RM120ET	RM120ET	RM150ET
	Quantity	2	1	1	2
Compressor	Model	C30VRT	C30PVRT	C30PVRT	C100L
	Quantity	2	1	1	1
Pumping Speed $l\,s^{-1}$)	N_2	17000	13000	13000	13000
	Ar	14000	10000	10000	10000
	H_2	25000	15000	16000	16000
	H_2O	39000	39000	39000	39000
Maximum throughput $(50Hz)\,(Pa \cdot m^3\,s^-1)$	Ar	4.1	3.0	3.0	Unmeasured
Pumping Capacity$(Pa \cdot m^3)$	Ar	8.1×10^5	5.8×10^5	5.8×10^5	5.8×10^5
Cool down time (50Hz)		150 min	170 min	230 min	Unmeasured
Power consumption (50Hz)/pump (kW)		10.0	6.0	6.0	4.2

Moreover, a pneumatic-drive G-M cryocooler was developed by Advanced Research Systems Inc. which requires an input power of 6.8 kW to cool down the second stage to 4.2K at a cooling power of 1.5W [35], putting the range of power demand of a cryopump to be between 4 to 7 kW.

2.2.3 Application in Hyperloop

Advantages of Cryopump

Cryopumps possess several advantages, namely being the most economic choice for pumps that can achieve ultra-high vacuum levels and black hole pumping speeds. Examples include DN1200; the biggest commercial pump with a speed of 60 $m^3\,s^{-1}$, and DN750, a customized cryopumps with 100 $m^3\,s^{-1}$ [4]. Furthermore, cryopumping operations are perfectly clean and oil-free, as well as requiring little maintenance due to having no mechanically moving parts [4, 20].

If a bath cryopump, which does not require any electric supply is taken into account, then it possesses the additional benefit of being safe from power breakdowns and free of vibration [4]. The different stages in cryopumping adds the possibility of selective pumping. While the difficulty in condensing hydrogen and helium is an issue raised in many cryopump designs, since hyperloop mainly aims to pump the air inside its tubes, a pure condensation pump without any sorbent may be a viable option. However, helium pumping is still beneficial due to the use of helium in detecting leaks [4].

Lastly, the large volume of air needed to be pumped out of hyperloop tubes is a surpassable challenge, as evidenced by the usages of cryopump to pump out chambers with volumes as large as 16000 to 22653 m^3 in thermonuclear fusion and space research respectively [38].

Disadvantages of Cryopump

On the contrary, the use of cryopumps in hyperloop is not suitable mainly due to the amount of time required for both cooling and regeneration. As shown in Figure **??**, **??** and **??**, a cryopump takes at least 1.5 hours to reach its working temperature, or as long as 4 hours, then another tens of minutes for regeneration. A study has discovered that the primary culprit for heat loss inside a G-M cryocooler is the non-equilibrium heat exchange between the helium gas in the cold cavity and the wall of its working cylinder, and thus proposed that a 2-fold increase in the heat exchange surface in the cold cavity will increase the cooling capacity by 25% based on simulated results [37], but this is still not ideal for a transportation system that emphasizes punctuality and availability at all times.

Additionally, while the main attraction of cryopumps is its capacity to reach an ultra-high vacuum, a pressure of 100 Pa is already sufficient for hyperloop, eliminating the need for the extremely low-pressure

range 100^{-5} to $10^{-10}\,Pa$ that cryopump provides. In summary, while the advantages of cryopumps make it a desirable choice for localized large chambers for conducting experiments, their application in a continuous operation over large distances at any given time like hyperloop is questionable.

2.2.4 Compatibility with other pumps

To combat the problems cryopumps face in order to be implemented in Hyperloop, a hybrid system using a combination of vacuum pumps is an essential requirement.

Turbomolecular pump

The main asset provided by this combination is the separation of the gases pumped between different vacuum pumps. For example, the Institute for Plasma Research developed a bath cryopump that is cooled using only liquid nitrogen, which focuses on condensing water vapour and nitrogen/air, while the pumping of hydrogen and helium is left to a turbo-molecular pump added into the system [38]. This combination of pumps is especially useful for pumping gases from a large chamber where nitrogen and water vapour are a major concern. An earlier study using the same cryopump also reduced the time needed to regenerate the pump [39]. The use of cryocoolers to aid in the pumping of water and hydrocarbon in turbomolecular pumps have also been investigated by various studies [4].

Dry screw pump

There has been no extensive study on the synergy between cryopumps and dry screw pumps, but the utilization of dry screw pumps alleviates the huge amount of gas needed to be pumped by cryopumps and may decrease the frequency of regeneration needed for cryopumps to function effectively.

2.3 Dry Screw Vacuum Pump

2.3.1 Mechanism

Dry screw pumps are dry, positive displacement pumps. "Dry" means the gas being transferred is not exposed to oil or water used in the pump, unlike wet pumps, which use these fluids as lubricants and seals. "Positive displacement" refers to the pump's operation by mechanically trapping a volume of gas and moving it through the pump, creating a low pressure on the inlet side [6].

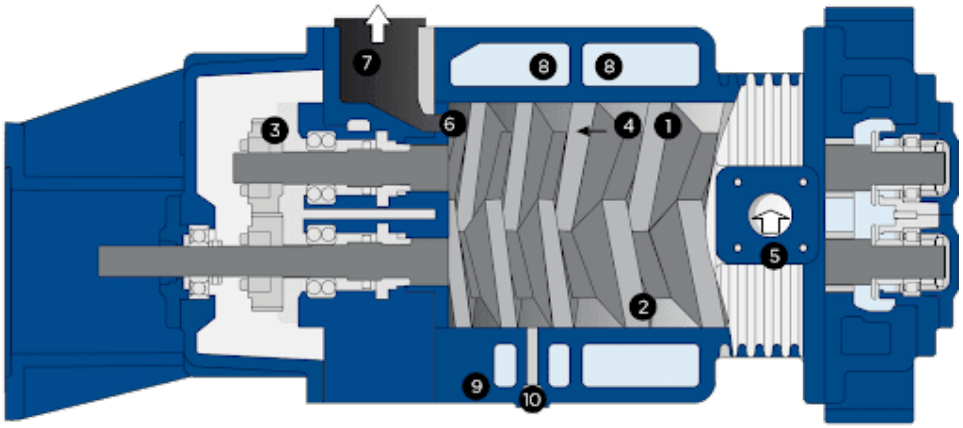

Figure 7: Dry Screw Pump Design [5]

A dry screw vacuum pump, as shown in Figure 7, consists of two parallel, non-contacting helical screw-shaped rotors, labelled (1) and (2) in the diagram, which rotate synchronously at high speeds thanks to precision gears (3). These rotors turn in opposite directions, capturing a quantity of gas at the inlet (5) and moving it towards the exhaust port (6) and into the exhaust channel (7). The stator walls (9) and the unique design of the intermeshing screws create compression chambers or pockets (4) that transport the gas.

Small clearances between the screws and the stator, as well as between the intermeshing screws, ensure minimal reverse leakage towards the inlet compared to the forward flow of gas generated by the screw pockets. The reverse flow of gas is controlled by the length of the sealing boundary, determined by the number of spirals and tight clearances. On pumps with a compression plate, a slight reverse expansion of gas into the screws occurs when the outlet valve or port is first exposed, which is quickly expelled as the trapped volume is progressively reduced to zero by the screws' action.

The reverse flow is primarily managed by the width of the "sealing lands" on the screw tips, which run close to the stator and minimize gas leakage.

Cooling is managed via the surrounding jacket (8). Pumps can be set up for direct or indirect closed-loop cooling. The latter has many advantages, as the plant's cooling water never comes into direct contact with the pump material, preventing jacket silting or corrosion due to poor water quality. A gas ballast port (10) is available, which can help warm up a cold pump, dry a wet pump faster, remove a flammable vapour from its flammable range, and clean solids out of a pump, especially during solvent flushing [5].

Some of the best dry screw pumps in the industry can achieve an ultimate pressure of approximately 1 Pa and a peak pumping speed of 566 $l\,s^{-1}$ [40, 41]. At ultimate pressure, these vacuum pumps have a power consumption of 4.1 to 4.6 kW [1], with the exact value depending on the model supplied [40, 42].

[1] The calculated mean of provided values is 4.4 kW [40, 42]

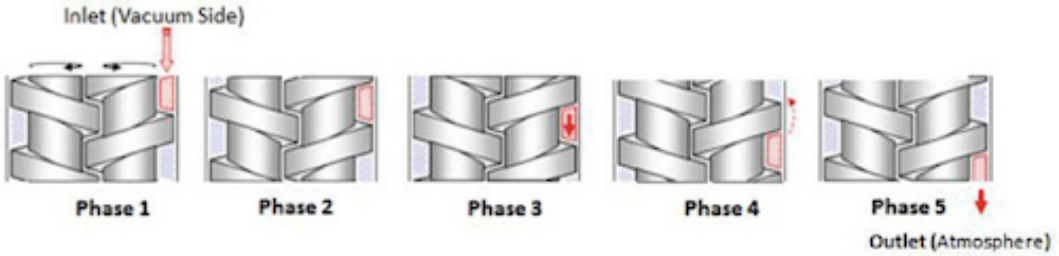

Figure 8: Phases of Gas Movement in a Dry Screw Vacuum Pump [6]

1. Phase 1: Gas Intake
   - Gas enters the inlet cavity.
   - The screw rotors rotate at high speed, creating inlet cavities between the rotors and the stator.
2. Phase 2: Sealing the Gas
   - As the screws continue to rotate, the cavity becomes sealed, isolating the gas from the inlet.
3. Phase 3: Gas Displacement
   - The relative motion of the screws moves the trapped gas pocket from the inlet toward the outlet along the pump axis.
4. Phase 4: Back Leakage
   - During gas transfer, some back leakage occurs where a small amount of gas leaks between the surfaces of the rotors and the stator, counteracting the direction of gas transfer.
5. Phase 5: Gas Expulsion
   - The trapped gas is transferred to the pump outlet at atmospheric pressure, completing the pumping action.

Dry screw pumps can be single-ended, where the gas enters at one end and exits at the other, or double-ended, where the gas enters in the middle and exits both ends of the pump [6].

2.3.2 Advantages

Employing dry screw pumps for a hyperloop track system comes with various benefits and drawbacks. The biggest and most impactful benefit is the oil-free operation.

The oil-free operation of dry screw pumps offers numerous advantages, making them a great choice for various industries that demand high efficiency, including the emerging hyperloop technology. By eliminating the need for oil, these pumps remove the risk of contamination and become significantly environment-friendly as they prevent oil leaks and spills, avoiding soil and water contamination and eliminating the need for hazardous waste disposal [43]. This contributes to a safer and cleaner working environment.

Andreas Tengler, Industrial Product Specialist at BOC Edwards, suggests the deployment of dry vacuum pumping technology, initially engineered for the semiconductor industry for its high cleanliness and operational efficiency, to various industrial and vacuum-based applications [44].

The efficiency of dry screw pumps is significantly improved by the absence of internal resistance and drag caused by oil. This results in superior energy performance and extends the equipment's lifespan, allowing for 10,000 to 15,000 hours of operation before servicing is required [45]. This extended operational life reduces the frequency of maintenance interventions, thereby lowering overall maintenance costs and minimising downtime which is critical for transportation systems These pumps can handle a wide

range of gases, including corrosive and particulate-laden gases, without the risk of oil reactions, making them versatile for diverse applications [44]. Additionally, oil-free operation helps industries comply with stringent environmental regulations, thus avoiding fines and legal issues.

The enhanced safety profile of dry screw pumps, due to the reduced risk of fires and explosions, and the improved product quality, especially in sensitive applications, further underscore their benefits. This is particularly important in hyperloop systems, which require maintaining a near-vacuum environment over long distances.

2.3.3 Disadvantages

The two most significant limitations of dry screw pumps are the high initial investment and the continuous need for backing pumps to maintain the desired vacuum strength and prevent leakage.

Dry screw pumps generally require a significant capital investment compared to traditional oil-lubricated pumps, ranging from thousands to tens of thousands of pounds [46, 47]. This higher initial cost stems from the advanced technology and precise engineering needed to produce these pumps. The design incorporates complex rotors that must maintain extremely tight clearances without making contact, which requires high manufacturing standards and quality materials. Additionally, high-quality coatings are often applied to the rotors to enhance their durability and resistance to various chemicals, further driving up the cost.

Another significant limitation is the necessity for backing pumps to support the primary dry screw pumps. This need arises because dry screw pumps alone cannot sustain ultra-high vacuum levels over long periods. Backing pumps, such as rotary vane or scroll pumps, are essential for achieving and maintaining the desired vacuum strength. These additional pumps handle the initial rough vacuum phase and maintain low pressure, allowing the dry screw pumps to operate efficiently in the high vacuum range.

This requirement exists because, although dry screw pumps are effective at maintaining a steady vacuum, they can struggle with challenges like gas ballast management and maintaining a seal-free environment to prevent leaks. Backing pumps help mitigate these issues by providing continuous support, thus ensuring the vacuum integrity of the system. However, this adds complexity and cost, as it necessitates the integration and maintenance of additional pumping systems.

2.4 Vacuum Leakage

Vacuum leakage remains a constant issue for a hyperloop as creating a perfectly tight tube is impossible. However, this will not pose a serious problem as the vacuum pumps can be used to counteract leakage. According to Rottlander et al, the ultimate pressure that can be achieved by a tube with pumping speed S_{eff} in a tube with a leakage rate of q_L is given by [48]:

$$P_{ult} = \frac{q_L}{S_{eff}}. \tag{1}$$

By assuming the leakage rate is caused by the porosity of the tube material, rather than a hole in the tube itself, Tudor and Paolone state the leakage rate of the tube can be determined according to Darcy's Law [49]:

$$q_L[\frac{m^3}{s}] = \frac{\pi \cdot k_{perm} \cdot L \cdot (p_{tube}^2 - p_0^2)}{\mu \cdot \ln(1 + \frac{\lambda}{d_{in}}) \cdot p_{tube}} \tag{2}$$

Where k_{perm} represents the air permeability of the tube material and μ represents the air dynamics air viscosity.

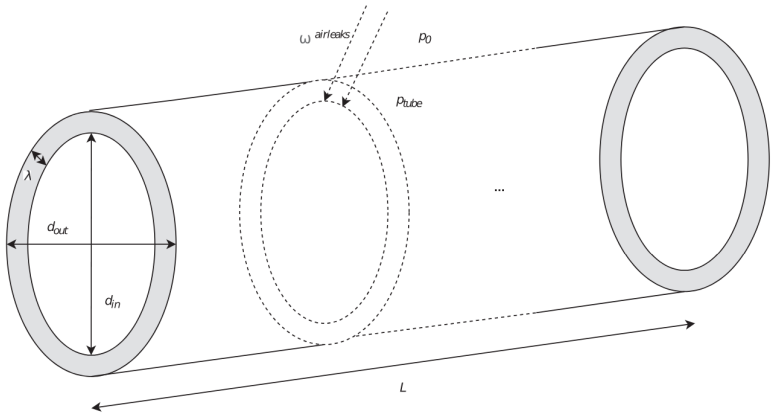

Figure 9: Simplified leak geometry of hyperloop tube

To ensure a stable vacuum, it is required that the leakage rate is less than or equal to the total pumping rate, namely:

$$q_l \leq N_{pumps} \cdot S_{eff} \tag{3}$$

If Equation 2 is expressed in terms of the linear number density of vacuum pumps, $\sigma \cdot L = N_{pump}$, then Equation 3 can be rearranged to find:

$$\frac{\pi \cdot k_{perm}}{\mu \cdot \ln(1 + \frac{\lambda}{d_{in}})} \frac{(p_{tube}^2 - p_0^2)}{p_{tube}} \leq \sigma \cdot S_{eff}. \tag{4}$$

The energy needed to maintain the vacuum over a unit length of the tube per unit of time can be expressed in terms of pump power as:

$$E_{vac} = \sigma \cdot P_{pump}. \tag{5}$$

Therefore, Equations 4 and 5 can be combined to determine the energy demand to maintain a unit length of vacuum as a function of p_{tube}:

$$\frac{\pi \cdot k_{perm}}{\mu \cdot \ln(1 + \frac{\lambda}{d_{in}})} \frac{(p_{tube}^2 - p_0^2)}{p_{tube}} \frac{P_{pump}}{S_{eff}} \leq E_{vac}. \tag{6}$$

The optimal solution will occur when the vacuum pumps just balance the leakage rate:

$$\frac{\pi \cdot k_{perm}}{\mu \cdot \ln\left(1 + \frac{\lambda}{d_{in}}\right)} \frac{(p_{tube}^2 - p_0^2)}{p_{tube}} \frac{P_{pump}}{S_{eff}} = E_{vac}. \tag{7}$$

2.5 Pump Comparison

Table 4: Comparison of Cryopump, Turbomolecular Pump, and Dry Screw Pump

Vacuum pump	**Main advantages**	**Main disadvantages**	**Energy Consumption** (kW)	**Maximum Pumping Speed** $(l\,s^{-1})$
Cryopump	• Can reach ultra-high vacuum strengths • Maintains a very clean and oil-free vacuum environment • Extremely low maintenance	• Requires regeneration • Has a large cooling time	4.2 - 6.8	10000
Turbomolecular pump	• Energy Efficient • Can reach ultra-high vacuum strengths	• Requires a secondary pump • Susceptible to vibrational damage	0.240	3000
Dry Screw Pump	• Extremely low maintenance • Environmentally Friendly due to lack of oil used	• Weaker vacuum strength • Requires a secondary backup pump	4.4	566

Using Equation 7, a direct comparison of the energy needed to maintain a unit length of vacuum can be created for the discussed vacuum pumps. Some assumptions are made regarding the tube characteristics. First, k_{perm} is assumed to be isotropic and a value of $5 \times 10^{-18}\,m^2$ [49]. The dynamic air viscosity was assumed to be $\mu = 1.85 \times 10^{-5} Pa \cdot s$ [49]. P_0 was taken to be atmospheric pressure, namely $P_0 = 101325\,Pa$. The thickness of the tube is quoted at 25 cm which is the lower bound for reinforced concrete in the tunnelling industry [50]. Lastly, the inner tube diameter is taken to be 3.30 m, as claimed in the hyperloop alpha paper [18].

Table 5: Comparison of Cryopump, Turbomolecular Pump, and Dry Screw Pump Energy Consumptions

Tube Pressure (Pa)	**Cryopump** (J)	**Turbomolecular** (J)	**Dry Screw** (J)
$10^{-}8$	5.5×10^{9}	N/A	N/A
10^{-6}	5.5×10^{7}	9.6×10^{6}	N/A
10^{-3}	5.5×10^{4}	9.6×10^{3}	N/A
1	5.5×10^{1}	9.6	9.3×10^{2}
100	5.5×10^{-1}	9.6×10^{-2}	9.3
1000	5.5×10^{-2}	9.6×10^{-3}	9.3×10^{-1}

As demonstrated in Table 5, a turbomolecular pump consistently performs the most energy efficiently in maintaining a vacuum. Due to a TMP requiring a forepump, as discussed in Section 2.1.3, the dry screw pump is recommended over the cryopump due to the minimal maintenance needed and the cryopump's long regeneration time. Therefore, the energetically optimized vacuum pump pairing for the hyperloop system is a turbomolecular and dry screw pump.

3 Compression System

3.1 Background

3.1.1 Kantrowitz Limit

The Kantrowitz limit is defined as the maximum speed at which a pod can travel before the fluid flow around the pod becomes choked and pressure shock waves are generated. [7]

When a hyperloop pod travels in an evacuated tube, there is a limit to the Mach number it can reach before choking the airflow. The Kantrowitz limit depends on the pod's blockage ratio, which is defined as:

$$\text{BR} = \frac{A_{pod}}{A_t} \text{ [7]} \tag{8}$$

Where:

$$BR = \text{Blockage Ratio}$$

The blockage ratio is a measure of how much area of the cross-section of the tube the pod occupies and is vital when designing an effective transport system.

This is due to the compressibility of air [51]. When pod speed exceeds this limit, pressure builds up in front of the pod, which subsequently affects the aerodynamics around the pod. Furthermore, as the flow around the pod becomes choked, it must compress the air in front, similar to a piston [7]. This adds additional pressure counteracting the motion of the pod as it moves forward.

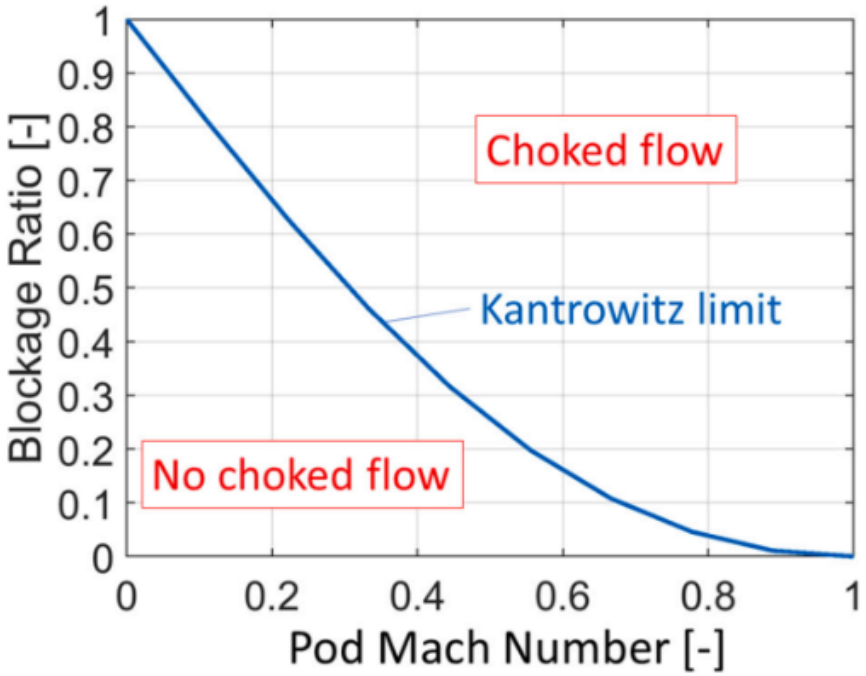

Figure 10: Graph showing the choking and non-choking regions according to the definition of the limit [7]

Choked flow greatly impacts the aerodynamics, speed and safety of the pod. Therefore, reducing the effects of the Kantrowitz limit is vital to the success of a hyperloop system. The Kantrowitz limit is a key principle affecting a hyperloop system's performance and efficiency. As shown in Figure 10, without

a compressor, avoiding choked flow inside the evacuated tube would either require a low blockage ratio or a low pod Mach number. As defined in Equation 8, a low blockage ratio would mean the cross-sectional area of the pod must be much smaller relative to the tube. This would mean that the pod size and subsequently its capacity to transport would be reduced. An alternate option is to increase the cross-sectional area of the tube. This would drive up the cost of maintaining the optimal tube pressure and the vacuum conditions, which will be discussed later in this section.

Low pod Mach number also presents an issue in the viability of the hyperloop as a mode of transportation. The higher the speed that the pod can travel the more beneficial it is as a transportation system. While pods with lower speeds were originally proposed by Musk et al [18] alongside high-speed pods, much of the literature focuses on simulations and calculations at high speeds.

3.1.2 Pressure waves

In addition to increased pressure, shock waves can also be generated in the rear and front of the pod due to choked flow within the tube [52]. At sufficiently large mach numbers, compression waves (CWs) and expansion waves (EWs) are generated [8]. As the pod accelerates, compression waves are generated in front of the pod, and expansion waves form at the rear of the pod [52].

Figure 11: Pressure wave contours as simulated in 2D and 3D CFD simulations. [8]

CWs propagate and cause an increase in pressure in the region in front of the pod. Conversely, EWs propagate from behind the pod and cause the pressure to decrease [8]. This causes an increase in the pressure gradient; subsequently, the total drag and the drag coefficient increase [53] which consequently affects the efficiency of the pod.

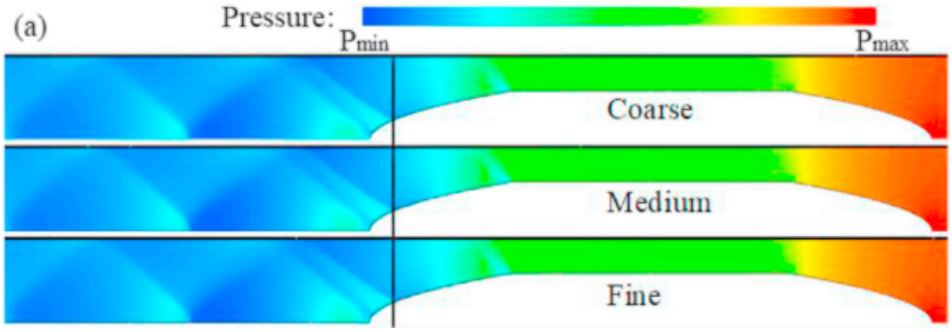

Figure 12: Pressure shock wave distributions done in a separate study [9]

Other forms of shock waves also become present at pod speeds beyond the Kantrowitz limit e.g. Mach numbers 0.6 and 0.8 at a blockage ratio of 0.2 [7]. Oblique Shock waves form, travelling with the direction of airflow.

Other challenges are presented to the aerodynamics and propulsion of the hyperloop system. Shock waves can cause damage, directly or through thermal stress, to the tube and pod structure over time [9]. This is highly undesirable in a hyperloop system which relies on its vacuum-like environment. A crack in the tube no matter the width could cause unexpected shock waves and highly under-expanded jets [22].

3.1.3 Compressor

An air compressor in a hyperloop pod provides an additional outlet of compressed air in front of the pod to flow out behind the pod [10]. This alleviates the choked flow which reduces the effects of the Kantrowitz limit and generated shock waves; thus, it benefits the pod in ways further that will be discussed in the next section. Furthermore, compressors as theorised by Musk, could be used to repurpose incoming air into air bearings or cushions which could be used as a method of levitation for the pod [18].

3.1.4 Implementation

A basic compressor that can be used in a hyperloop system requires a compressor at the nose of the pod which takes in the airflow and a nozzle equipped at the tail of the pod. This has been modelled by Bizzozero et al [7] as a simple tube or channel where air can flow through the pod.

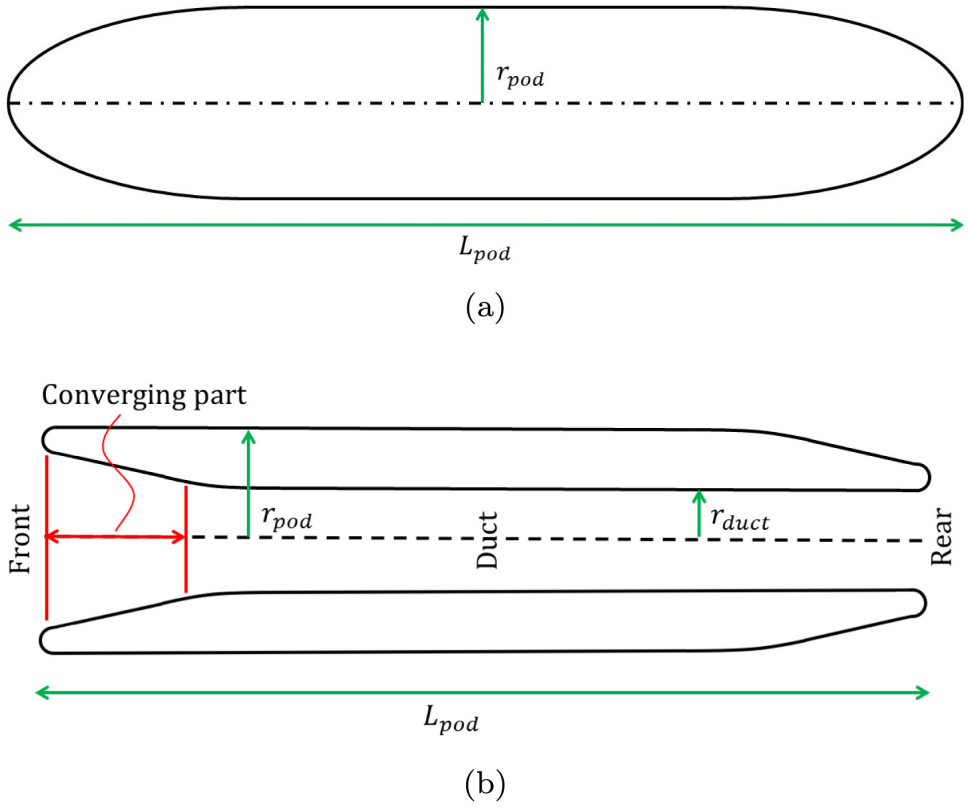

Figure 13: Initial simple model of compressor. [7]

However, the main type of compressor studied, through simulations and calculations, in current literature is the axial compressor.

An axial compressor consists of an intake port where the air enters and is propelled by the rotating rotor blades [54], causing the air to diffuse. As previously mentioned, axial compressors are the most studied type of compressor and would reflect realistic conditions rather than a simple duct through the middle of the pod.

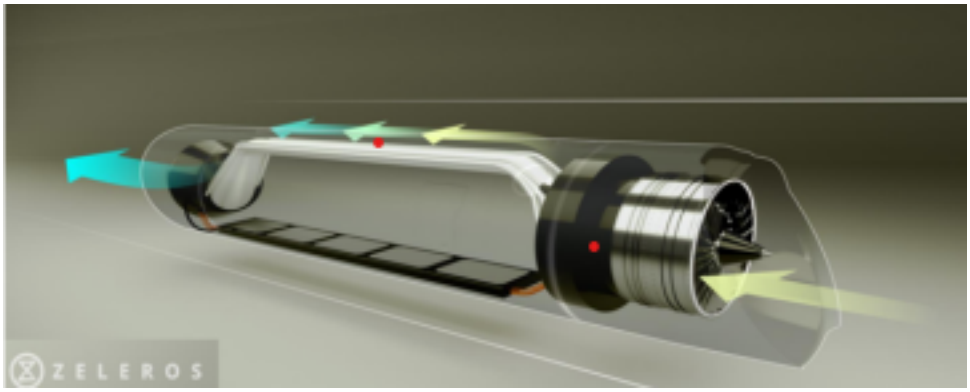

Figure 14: Axial Compressor model [10]

As modelled in Figure 14, the compressor uses a bypass for air to flow from the front of the pod to the rear while leaving room for the payload or passengers within the pod. This section will discuss the simulation results of both models.

3.2 Advantages

3.2.1 Speed

Under the same tube conditions as a pod without a compressor, a simulated case for a pod with a compressor travelling at 700 $km\,h^{-1}$ could be operated at blockage ratios 0.5 - 0.6 compared to a pod without a compressor which experienced the effects of the Kantrowitz limit at blockage ratios of 0.1 - 0.2 [25]. This is due to the overall impact it has on the aerodynamics of the pod most notably the pressure distribution inside the tube; delaying the transonic effects and mitigating the induced pressure in front of the pod [25]. The compressor is vital in allowing the pod to operate at high speeds without compromising its blockage ratio.

As discussed in Section 3.1.2, pressure waves and the pressure gradient directly affect the speed limit at which the pod can operate with the risk of damage.

3.2.2 Pressure

As discussed in Section 3.1.4, the air compressor transfers the compressed air from in front of the pod to behind the pod. This reduces the drag on the pod as the pressure differential between the front and the back of the pod is more evenly distributed, reducing the effects of the shock waves that can form around the pod in addition to the ones in front.

The reduction of the pressure differential also reduces the drag caused by the passage flow around the pod.

Table 6: Reduction in pressure and its subsequent pressure ratio for different cases. [7]

Case	p in front, deactivating compressor (Pa)	Compressor pressure ratio	p in front, activating compressor (Pa)	Reduction (%)
BR 0.56, MA 0.4	16,450	2.9	11,200	32
BR 0.56, MA 0.6	25,100	3.5	15,900	36.7
BR 0.56, MA 0.8	33,750	3.9	20,650	38.8
BR 0.72, MA 0.4	26,850	2.7	14,950	44.3
BR 0.72, MA 0.6	40,900	3.4	20,200	50.6
BR 0.72, MA 0.8	55,100	3.9	25,500	53.7

It is important to note that the values simulated and the resulting compressor pressure ratios are still lower than the 20:1 figure initially proposed by Musk [18], the highest value being simulating being 4:1 [7]. High ratios, as Musk proposed, remain an area for future research as previous computational models, such as that used in the study by Bizzozero et al, have experienced instability in simulation analysis [7]. To increase the ratio, more power would be required to operate a compressor with higher strength.

3.2.3 Power Consumption

The total power consumption of a hyperloop system can be modelled with a degree of simplification by considering the following sources of power consumption:

- Power needed to maintain the vacuum, P_{vac}
- Power usage of the compressor, P_{compr}
- Power usage of propulsion (in most simulated cases a Linear Induction Motor, LIM is considered), P_{LIM}

The total power P_{tot} can then be defined as.

$$P_{tot} = P_{vac} + P_{compr} + P_{LIM} \tag{9}$$

For simplicity, it can be assumed that the power needed to maintain the vacuum would be the same given the same initial conditions which then leaves the total variable power as follows [7]:

$$P_{tot} = P_{compr} + P_{LIM} \tag{10}$$

Note that optimising vacuum pressure is another factor affecting the efficacy of the compressor, which will be discussed in Section 3.6.

Generally, the power consumption for a pod equipped with a compressor decreases, relative to a pod without a compressor, as speed increases. However, this is only the case at sufficiently high blockage ratios. For example, at Mach number 0.8 as simulated blockage ratios of 0.4 and lower experience a gain in power consumption instead of a reduction.

This is ideal as the larger percentages of reduction in power consumption for the pod equipped with a compressor typically occurred at higher blockage ratios and Mach numbers; in line with the goal of high-speed travel in a hyperloop system. The optimal pressure for reduction in power consumption was found to be the case where B.R. = 0.72 and Ma = 0.8, which yielded a decrease in the power consumption coefficient C_{power} of 44%. [7] This was done with the initial conditions involving 10132 Pa or approximately 0.1 atm.

In a different study by Lluesma-Rodríguez et al using computational fluid dynamics simulations, the reduction in pod power consumption when equipped with a compressor was also demonstrated with pod conditions of 500 $km\,h^{-1}$ and 700 $km\,h^{-1}$ speeds; 0.404 and 0.566 $Mach$ respectively. With the reference vacuum condition of also set to 0.1 atm pressure.

The efficiency of the compressor in reducing power, if taken as the percentage reduction in drag and or power, remains relatively similar between the ranges of 0.01 atm and 0.1 atm, with the highest rate being up to approximately 47.5% [7]. However, the power required to achieve similar results will be much lower in lower-pressure environments as demonstrated in Figure **??**. This means a balance between the compressor strength and vacuum strength will need to be optimised. A decrease in tube pressure may be something more cost-effective [18]. However, the scalability may be negatively affected.

Table 7: Drag comparison between pods with and without compressors at different tube pressures [22]

P_{tube} (Pa)	Mach	Drag w/o compressor (N)	Drag w/ compressor (N)	converged $(\dot{m}\,kg\,s^{-1})$
100	0.7	243	115	0.124
	0.8	299	123	0.140
	0.9	351	134	0.157
300	0.7	666	305	0.366
	0.8	833	342	0.412
	0.9	975	370	0.463
500	0.7	1075	495	0.607
	0.8	1354	561	0.683
	0.9	1580	605	0.767
1,000	0.7	2063	978	1.204
	0.8	2622	1097	1.356
	0.9	3049	1180	1.521
5,000	0.7	9673	4729	5.961
	0.8	12474	5244	6.698
	0.9	14416	5614	7.500
10,000	0.7	18944	9272	11.896
	0.8	24538	10325	13.335
	0.9	28306	11042	14.933

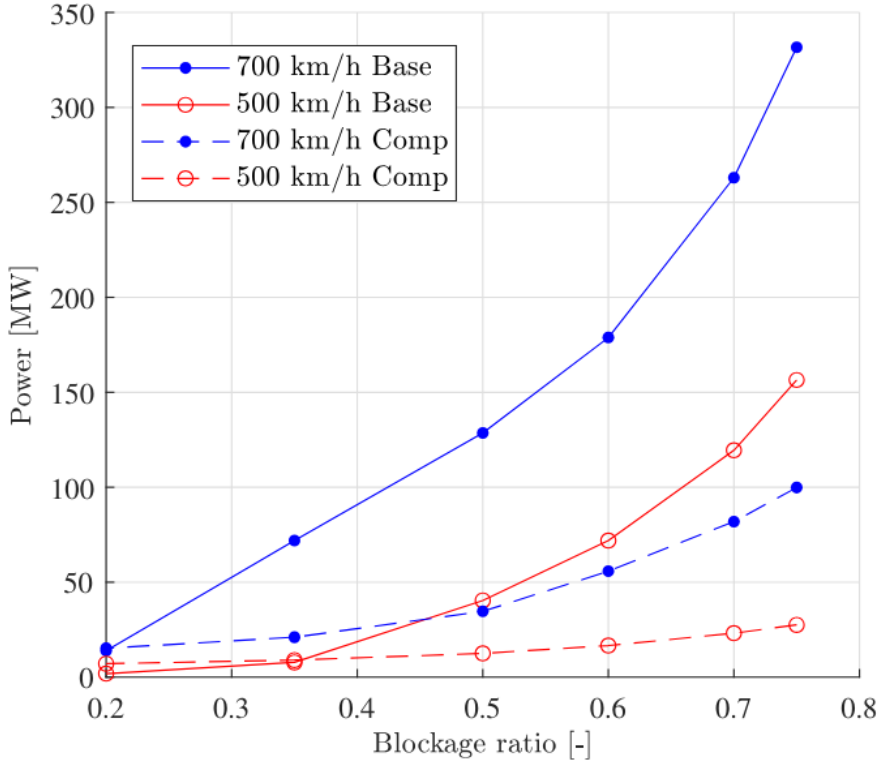

Figure 15: Power consumption for pods with and without compressors [11]

Both studies in this case modeled the pod without a channel for air below the pod i.e. not using levitation, which could be a potential avenue for even greater benefits.

3.3 Disadvantages

3.3.1 Temperature

The implementation of a compressor, while has been shown to decrease the drag and hence the overall temperature of the pod, presents a challenge for specific parts in the pod itself. In a study by Zhou et al [9], the geometry of the axial channel or radial gap, as methods of implementing a compression system, requires careful consideration as during temperature on the surface near the channels can increase significantly, especially during the deceleration phase [9]. The maintenance of this would come at a high cost and depending on the materials used to implement the compressor, the longevity of the compressor will be affected.

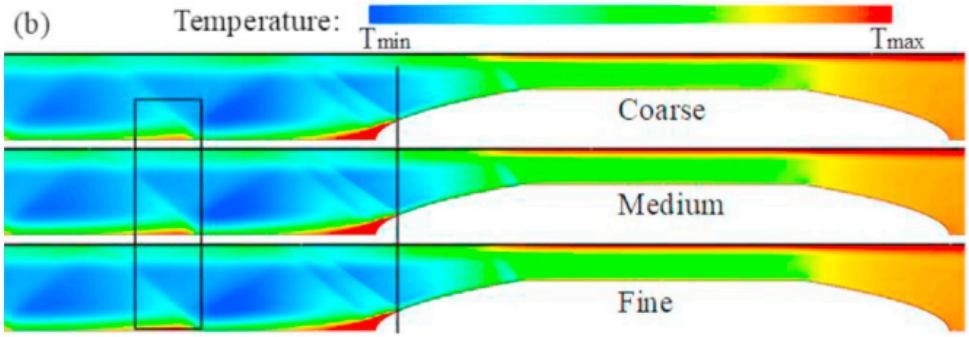

Figure 16: Temperature contours around the pod with a difference of 100K between the maximum and minimum temperature.

Furthermore, as the high-temperature air of up to $400K$ enters the channel, it must also be cooled down [9]. This is another demand that rises when travelling at high speeds. The requirement of power can be expressed as:

$$P_{compr} = \dot{m} c_p \Delta T_0 \tag{11}$$

Where $\dot{m}$ is the mass inlet flow, c_p is the specific heat capacity at a given pressure and ΔT_0 is the change in temperature of the air [7]. The change in temperature around the could also affect the value of c_p, however, this is insignificant in the grand scheme as changes in the heat ratio c_p/c_v can be as little as 0.05 between $400K$ and $300K$, for example.

3.4 Feasibility and Challenges

In the current climate, implementing a compressor into any hyperloop system will be vital and is the most optimal way of addressing the Kantrowitz limit and the challenges that come with the barrier. To study the feasibility of implementing this subsystem, the costs and the challenges must be considered. For one, Musk originally proposed that in a hyperloop system spanning from San Francisco to Los Angeles, the cost of a fan-type axial compressor would be at least $275000 [18] and would make up at least 1800 kg of the total mass of the pod. Currently, an axial compressor has not been implemented successfully into a real-life model of a hyperloop pod and has only merely been simulated. However, this compressor has been in use in other areas of transportation, most notably the aerospace industries for decades [54].

It can be concluded that the main challenges of implementing a compressor will come with:

- Finding the optimal geometry of the axial channel.
- Fitting a powerful enough cooling module.
- Operating at an optimum vacuum strength and pressure.

These remain the questions that should be explored further in research to develop a working compression system.

3.5 Air Bearings for Levitation

3.5.1 Mechanism

The utilisation of an air compressor in the hyperloop system can be further strengthened by diverting the flow of air underneath the pod for levitation, as Musk suggested in his Hyperloop alpha paper [18].

Levitation of the pod would allow the hyperloop pod to gain a competitive edge over other modes of transportation by minimising rolling and contact friction [12].

The purpose of this is to reduce friction between the pod and the tube walls. Although there are concerns about viscous drag being produced between the air cushion and the tube walls, the drag generated is negligible, with estimates of only $140N$ of resistive force being generated at Mach 0.99 [55].

The proposition of air bearings can be visualised by an air hockey table. A constant flow of air is constantly projected through small holes, forming an air cushion between the hockey puck and the table. Similarly, numerous air bearings can be attached to the underside of the hyperloop pod, creating a similar air cushion, and effectively causing the pod to levitate.

Air bearings can be split into two classes: aerodynamic (requiring relative motion to generate air film) and aerostatic (requiring an external pressure source to generate air film) [56]. Aerodynamic air bearings are generally proposed in the designs of the hyperloop concept. To generate the air film, this type of bearing simultaneously shears and squeezes the gas between the surfaces in relative motion. As the speed of the pod increases, air molecules accumulate into the gap between the surfaces, creating a pressure gradient, which induces a load-carrying effect, levitating the pod [56]. At hypersonic velocities, the pressure is great enough to support large weights, making it ideal for the hyperloop system. This air is supplied via the axial compressor connected to an air reservoir [18].

3.5.2 Analysis

To simplify the analysis, the air bearing can be assumed to be rectangular with a length l and width a as shown in Figure 17. Since the gap height h is much smaller than the dimensions of the air bearing, lubrication theory can be applied to this flow scenario [13].

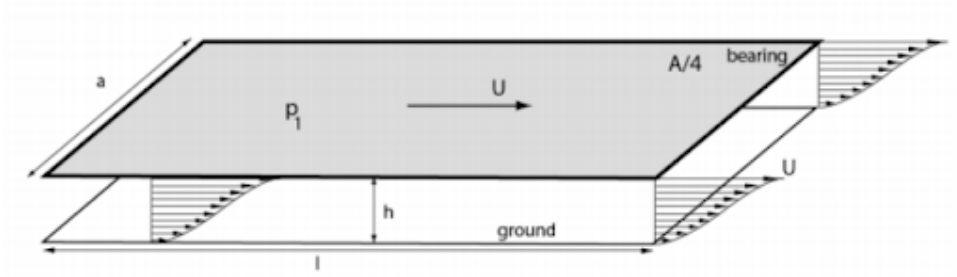

Figure 17: Air bearing diagram [12]

Under lubrication theory, the Navier-Stokes equations can be integrated to give the parabolic velocity profile:

$$u(y) = \frac{1}{2\mu}\frac{\partial P}{\partial x} \cdot y(y-h) \tag{12}$$

where u is the velocity profile between the air bearing and ground, μ is the kinematic viscosity, $\frac{\partial P}{\partial x}$ is the pressure gradient along the flow direction, and h is the gap between the air bearing and the ground [13]. By integrating the velocity profile and assuming that the flow is incompressible, the mass flow rate $\dot{m}$ can then be calculated [13]:

$$\dot{m} = \Delta P \frac{\rho h^3 a}{12\mu l} + U \cdot \frac{\rho h a}{2l}. \tag{13}$$

From this, the effects on the mass flow rate by the design parameters, the pressure difference across air bearing ΔP, air bearing gap height h, air bearing width a, air bearing length l, and pod speed U, can be seen. The air-bearing gap height scales as cubic whilst the other parameters scale linearly, suggesting

that the air-bearing gap height is the driving parameter of the system. By fixing the width of the air bearing, varying the length of the air bearing is equivalent to varying the area of the air bearing, so the change in the mass flow rate can be investigated as a function of the air bearing area and the gap height, as shown in Figure 18 [13].

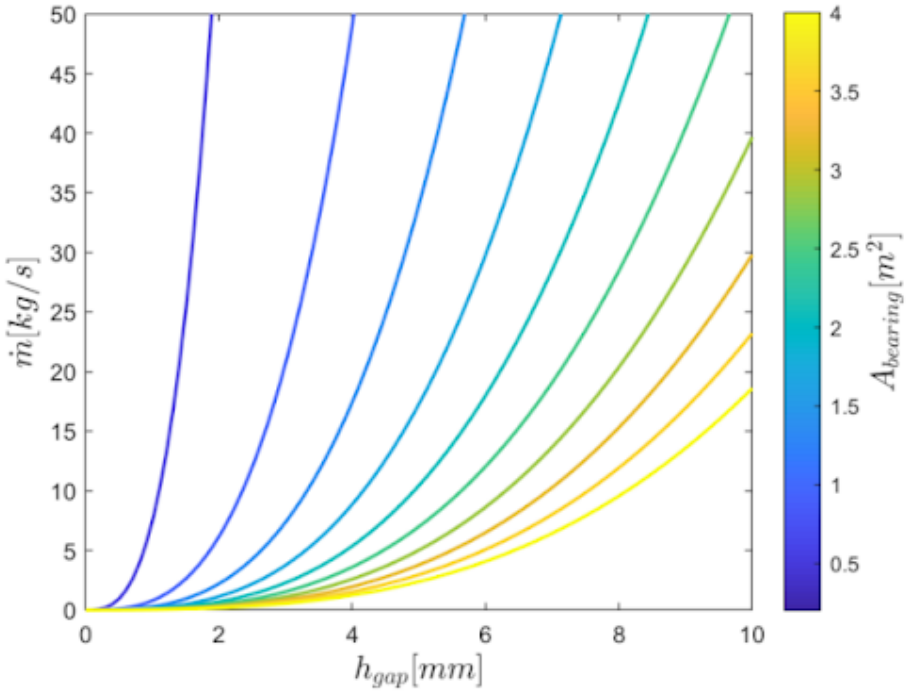

Figure 18: Air bearing mass flow rate as a function of bearing area and gap height [13]

3.5.3 Power Requirements

Due to the friction between the air molecules and the tube within the air gap, viscous drag is also produced, which requires additional propulsive power to oppose this drag force. This propulsive power requirement scales proportionally to the square of the velocity of the pod and inversely proportional to the levitation gap height [12]. This suggests that larger gap heights require less additional power requirements, which is expected since a smaller gap height results in higher stress at the wall and hence, a larger power requirement [12]. Compared to other levitation/locomotion methods such as magnetic levitation and wheeled systems, air bearings still have the lowest overall power requirement, which is ideal to minimise energy consumption.

3.5.4 Feasibility

Figure 18 shows that for an air gap height of $5mm$, a minimum mass flow rate of 2.4 kgs^{-1} is required with an air-bearing area of 4 m^2. Assuming a speed of 450 mph, the volume of gas required to be stored on the Hyperloop pod for a given journey can be estimated. For example, the distance between Edinburgh and London is 332 miles (air line) resulting in a journey time of $2656s$. As a result, 6374 kg of air would need to be stored, occupying a volume of 4930 m^3, which is clearly unfeasible. Compressing this air to 3000 psi, similar to that in submarines, a volume of 24 m^3 is occupied instead which is more reasonable. However, the cost of compressing this volume of air for every trip is expensive and inevitably unfeasible at large scales. Alternatively, the gap height can be reduced in order to reduce the mass flow rate required. However, safety concerns arise as small vibrations at high speeds could result in abrasions between the pod and the tube, leading to rapid deterioration of the pod [13]. Additionally, a compression ratio of 20:1 via the axial compressor is estimated to be required, which is currently a challenge within the compressor design industry [18]. Consequently, it can be concluded that air bearings are unfeasible for use in the Hyperloop system, unless these complications can be overcome.

3.6 Vacuum Optimisation

Relating the drag acting on the pod to the energy needed to maintain a vacuum will provide an estimate for the optimal vacuum strength of the hyperloop tube. Given that aerodynamic drag increases linearly with tube pressure, a line of best fit was used on the data given in figure **??** [57]. This is demonstrated in Figure 19.

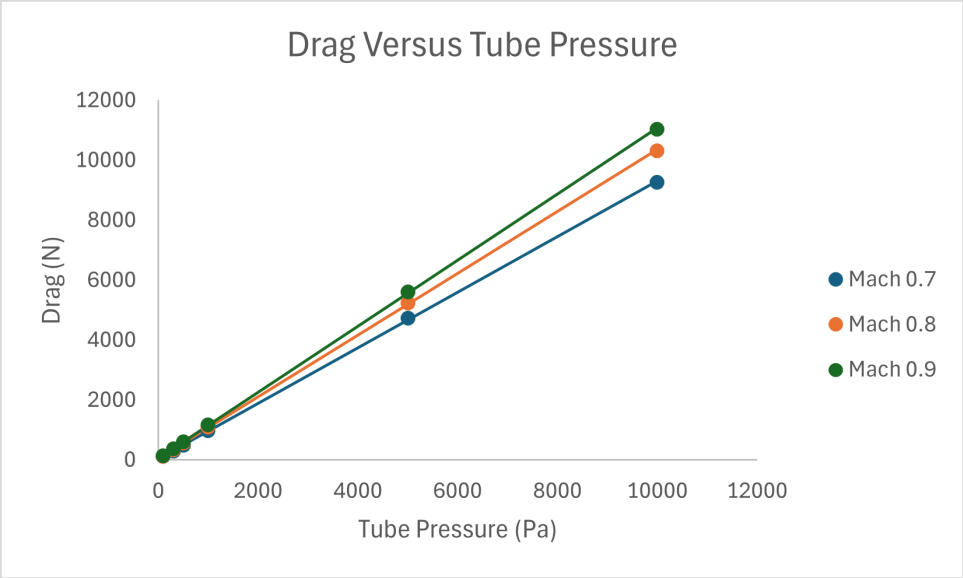

Figure 19: Linear Model of Drag versus Tube Pressure

The pod speed is assumed to be $0.8\,M$ as this is the predicted optimal speed [58]. Pod headway time is assumed to be $5\,min$ [2] which is the time quoted by Ingo A. Hansen to be the minimum time required to ensure adequate safety standards [59]. Assuming the pod acceleration to be constant at $1.5ms^{-2}$ until reaching steady-state speed, the spatial pod density is then determined to be $\frac{1}{57.2}$ pods per km using:

$$\sigma_{pod} = \frac{1}{v_{pod} * (300 - t_{acc}) + \frac{1}{2}at_{acc}^2} \tag{14}$$

where t_{acc} is the time it takes for the pod to accelerate to steady-state speed.

Therefore, the energy lost due to drag [3] per unit length, and consequently, the energy supplied by the propulsion system can be determined using:

$$E_{drag} = \sigma_{pod} \cdot F_{drag}. \tag{15}$$

The total energy consumption for a pod travelling in a given pressure can be determined as:

$$E_{tot} = E_{vac} + E_{drag} \tag{16}$$

Where E_{vac} can be determined using Equation 7 and E_{drag} can be found using the predicted model in Figure 19 and Equation 15.

Table 8: Calculated Energy Consumptions for Various Tube Pressures

[2] Headway time is proportional to optimal headway time, therefore a shorter headway will require a stronger vacuum.
[3] Steady state conditions were assumed for these calculations.

Tube Pressure (Pa)	$E_{drag}(J\,m^{-1\,s^{-1}})$	$E_{vac}(J\,m^{-1}\,s^{-1})$	$E_{tot}(J\,m^{-1}\,s^{-1})$
10^{-6}	8.18×10^{-4}	9.55×10^{6}	9.55×10^{6}
10^{-5}	8.18×10^{-4}	9.55×10^{5}	9.55×10^{5}
10^{-4}	8.18×10^{-4}	9.55×10^{4}	9.55×10^{4}
10^{-3}	8.18×10^{-4}	9.55×10^{3}	9.55×10^{3}
10^{-2}	8.18×10^{-4}	9.55×10^{2}	9.55×10^{2}
10^{-1}	8.20×10^{-4}	9.55×10^{1}	9.55×10^{1}
1	8.36×10^{-4}	9.55	9.55
10^{1}	9.98×10^{-4}	9.55×10^{-1}	9.56×10^{-1}
10^{2}	2.62×10^{-3}	9.55×10^{-2}	9.81×10^{-2}
10^{3}	1.88×10^{-2}	9.55×10^{-3}	2.84×10^{-2}
10^{4}	1.81×10^{-1}	9.46×10^{-4}	1.82×10^{-1}

As shown in Table 8, a minimum total energy occurs between $p_{tube} = 100Pa$ and $p_{tube} = 10000Pa$. Table 9 showcases a more precise table of calculated values.

Table 9: Expanded Energy Consumptions for Various Tube Pressures

Tube Pressure (Pa)	$E_{drag}(J\,m^{-1}\,s^{-1})$	$E_{vac}(J\,m^{-1}\,s^{-1})$	$E_{tot}(J\,m^{-1}\,s^{-1})$
10^{2}	2.62×10^{-3}	9.55×10^{-2}	9.81×10^{-2}
3×10^{2}	6.22×10^{-3}	3.18×10^{-2}	3.81×10^{-2}
5×10^{2}	9.82×10^{-3}	1.91×10^{-2}	2.89×10^{-2}
7×10^{2}	1.34×10^{-2}	1.36×10^{-2}	2.71×10^{-2}
9×10^{2}	1.70×10^{-2}	1.06×10^{-2}	2.76×10^{-2}
1.1×10^{3}	2.06×10^{-2}	8.68×10^{-3}	2.93×10^{-2}
1.3×10^{3}	2.42×10^{-2}	7.34×10^{-3}	3.16×10^{-2}

Therefore, for a hyperloop system in which a turbomolecular pump is used and the pod travels at $0.8\,M$ with a compression system, table 9 indicates that the optimal tube pressure lies between 500 and 1000 Pa. This differs greatly from the initial value of $100\,Pa$ predicted by Elon Musk [18]. A more accurate value can be reasonably determined with a computational fluid dynamic simulation incorporating accurate tube characteristics and compression mechanics. In addition to this, these calculations did not consider the propulsion supplied by the compression system.

4 Pod Design

Despite travelling in a near vacuum, the high speed of transport creates interesting aerodynamics surrounding the pod as discussed in Section 3. The existence of pressure shockwaves surrounding the pod mandates the implementation of an axial compressor to reduce the pressure drag. The design of the pod should consider the aerodynamics of this problem, emphasizing a head shape that can include a compressor duct. Additionally, the tail and head shape should be designed to minimise drag and maximise lift. For completeness, the choice of material should be investigated by features critical to its performance on the hyperloop pod including thermal and electrical conductivity, stiffness, and production capability.

To ensure practicality, the pod interior should be considered when designing. The features to be analysed when designing the interior primarily include length, seating and freight arrangement, and seating capacity. There are additional features to be investigated, such as windows and interior lighting however, the primal aspects are the ones most relevant to energy consumption. Before designing, it should be determined whether the pod will be used for passengers, freight, or both.

In this paper, an initial design for a comprehensive hyperloop pod was created. An emphasis on energy consumption and sustainability was placed on decisions concerning the pod design. The exterior was designed to minimize drag acting on the pod and maximize lift produced by fluid flow. The interior was analyzed to minimize the energy consumed per passenger per trip. The interior was also investigated as a modular system in which both freight and passengers can be transported with a single pod, reducing the material and energy demand of pod construction. Finally, aluminium alloy, PAEK, and PEEK were investigated as potential pod materials based on their physical characteristics and sustainability.

4.1 Exterior Design

4.1.1 Background

Significant technical hurdles must be overcome before the hyperloop can viably operate at its desired speeds and degree of evacuated tube pressure. The complex aerodynamics involved, including compressibility effects, shock wave-boundary layer interactions, choked flow conditions, and intricate shock patterns, pose major design challenges. Aerodynamic drag has been shown to increase dramatically with pod speed, tube-to-pod area ratio, and operating pressure, while exhibiting more complex dependencies on pod geometry. Careful aerodynamic optimisation of the pod shape is therefore crucial for minimising drag and achieving the hypervelocity performance promised by the hyperloop concept.

Previous studies have investigated pod shapes aimed at reducing drag, but most have focused on subsonic speeds far below the 1,200 $km\,h^{-1}$ hyperloop target. Other work has only considered the nose or tail geometry in isolation or failed to examine the potentially stabilizing effects of design-induced aerodynamic lift forces. At the time of this study, no previous research has performed a comprehensive multidisciplinary design optimization of the complete hyperloop pod shape that accounts for both drag minimization and lift maximization objectives under the compressible, turbulent flow conditions present in the near-vacuum hyperloop operating environment.

4.1.2 Theory

Computational Techniques for Studying Airflow

While there is limited research specifically focused on the airflow dynamics surrounding hyperloop pods, a wealth of knowledge can be gleaned from studies on other high-speed vehicles, particularly trains. Researchers have employed various methods, including experimental setups and computational techniques, to investigate airflow patterns around trains in open environments, in the presence of wall interference, and within confined spaces such as tunnels. Due to the high costs and time-consuming nature of experimental approaches, computational methods have gained popularity in recent years, providing accurate results comparable to experimental findings.

Computational Methods

Reynolds-Averaged Navier-Stokes (RANS)

RANS has emerged as one of the most widely used computational techniques for studying the aerodynamics of high-speed trains in open environments, proving to be a reliable and accurate method. Studies using RANS have also explored the motion of trains through constrained spaces, revealing the formation of vortices at the front of the train as it enters a tunnel, resulting in significant drag. Furthermore, researchers have found that the pressure generation at the train's front due to vortex formation is proportional to the square of the train's speed. More complex pressure patterns have been investigated when multiple trains move through a tunnel simultaneously.

Large Eddy Simulation (LES) and Detached Eddy Simulation (DES)

LES, introduced in 1962, is a well-established technique for modelling turbulent flows. It has been extensively used in various applications. DES, on the other hand, is employed for more complex flow situations, such as studying the wake region behind high-speed trains. These methods provide valuable insights into the intricate flow dynamics associated with high-speed vehicles.

Direct Numerical Simulation (DNS)

DNS is a highly accurate method that resolves the smallest turbulent phenomena and fastest fluctuations by utilizing a very fine mesh and small time steps. While DNS does not require additional modelling to resolve turbulence, it comes with a high computational cost, especially for high Reynolds numbers in complex geometries.

Other Methods

In addition to the aforementioned techniques, researchers have explored other methods such as the Riemann variables method to predict pressure waves generated by high-speed trains inside tunnels.

4.1.3 Numerical and Optimization Algorithms

The hyperloop pod aerodynamic design problem involves multiple conflicting objectives - maximising the leading nose lift to support the pod's weight while minimising the overall drag to reduce energy consumption and operating costs. This multi-objective optimisation must be performed within geometric constraints to ensure the pod's structural integrity and operational safety.

Maximising nose lift is crucial for stable levitation dynamics by counteracting the pod's weight and preventing excessive tube wall interactions that increase friction drag. However, excessive lift can lead to control instabilities, so an upper limit based on the pod's weight and control authority must be enforced. Within the current multidimensional design space, maximising lift toward this limit is desirable for offsetting weight.

Minimising overall drag directly reduces the propulsive power requirements. The major drag components are pressure drag on the nose/tail and skin friction drag over the pod surface. Careful shaping is needed to minimise adverse pressure gradients that trigger flow separations causing pressure drag peaks.

Direct high-fidelity aerodynamic shape optimization with a global optimizer like genetic algorithms is computationally intractable due to a large number of design variables and the high cost of solving the Navier-Stokes equations with turbulence modelling for each evaluation. Instead, a surrogate-based optimization approach is employed.

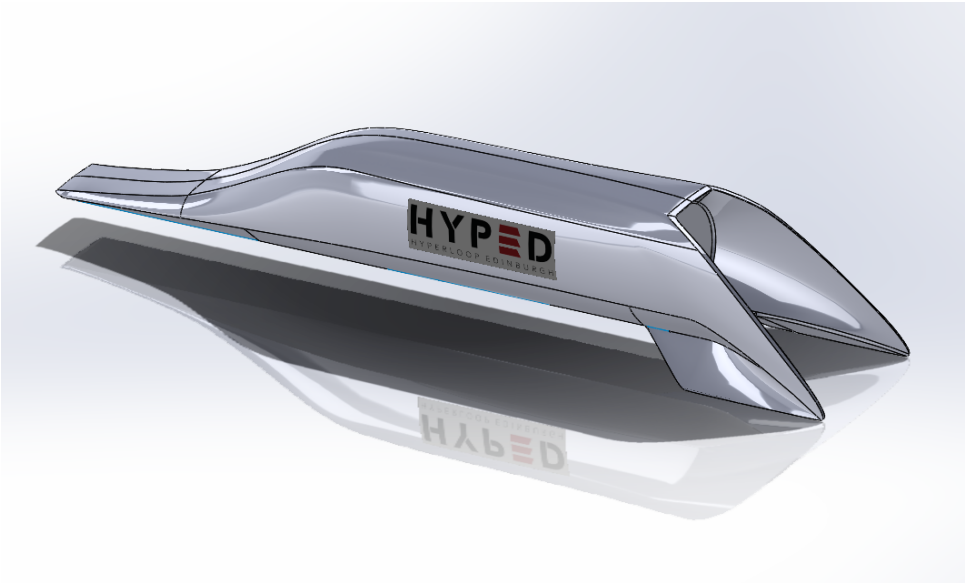

Figure 20: Hyperloop Pod Design

CFD Solver

The steady Reynolds-Averaged Navier-Stokes (RANS) computational fluid dynamics (CFD) solutions are obtained using the industry-proven commercial solver STAR-CCM+. This solver employs a finite volume discretization approach for the integral form of the RANS equations, offering excellent robustness, accuracy, and parallel scalability. Such a feature is commonly available in most commercial CFD software packages like ANSYS and Simscale.

To accurately predict the flow separations induced by adverse pressure gradients, the shear stress transport (SST) k-ω turbulence model is employed. This model combines the strengths of the standard k-ω model, which provides accurate boundary layer solutions near walls, with the standard k-ϵ model in the freestream region. This hybrid approach mitigates the excessive shear stress predictions associated with the baseline k-ω model in adverse pressure gradient conditions.

Alternatively, the commercial CFD software ANSYS Fluent, equipped with a density-based solver, is utilized to solve the governing equations of fluid dynamics. These equations encompass the continuity equation, which describes the conservation of mass, the Navier-Stokes equations, which represent the conservation of momentum, and the energy equation, which governs the conservation of energy, all expressed in terms of density.

$$\frac{\partial \rho}{\partial t} + \frac{\partial}{\partial x_i}(\rho u_i) = 0 \tag{17}$$

$$\frac{\partial}{\partial t}(\rho u_i) + \frac{\partial}{\partial x_i}(\rho u_i u_j) = -\frac{\partial P}{\partial x_i} + \frac{\partial}{\partial x_j}\left[\mu\left(\frac{\partial u_i}{\partial x_j} + \frac{\partial u_j}{\partial x_i} - \frac{2}{3}\delta_{ij}\frac{\partial u_k}{\partial x_k}\right)\right] + \frac{\partial}{\partial x_j}\left(-\rho\overline{u_i' u_j'}\right) \tag{18}$$

$$\frac{\partial}{\partial t}(\rho E) + \frac{\partial}{\partial x_j}\left[u_j(\rho E + P)\right] = \frac{\partial}{\partial x_j}\left[(k_{eff})\frac{\partial T}{\partial x_j}\right] + \frac{\partial}{\partial x_j}\left[u_i \mu_{eff}\left(\frac{\partial u_i}{\partial x_j} + \frac{\partial u_j}{\partial x_i} - \frac{2}{3}\delta_{ij}\frac{\partial u_k}{\partial x_k}\right)\right] \tag{19}$$

i, j, k = 1, 2, 3

where ρ, u, P, T, and μ are the fluid density, velocity, pressure, temperature, and viscosity, respectively. E is the specific internal energy, and k_{eff} and μ_{eff} are the effective thermal conductivity and dynamic viscosity, respectively. In this study, the air is assumed to be compressible, viscous, and an ideal gas. The air density thus obeys the ideal gas law as follows:

$$\rho = \frac{p}{RT} \tag{20}$$

where $R = 287.058$ J/kg $\cdot$ K is the individual gas constant, and p and T are the pressure and temperature of air, respectively.

Turbulence Kinetic Energy:

$$\frac{\partial k}{\partial t} + U_j \frac{\partial k}{\partial x_j} = P_k - \beta^* k\omega + \frac{\partial}{\partial x_j}\left[(\nu + \sigma_k \nu_T)\frac{\partial k}{\partial x_j}\right] \tag{21}$$

Specific Dissipation Rate:

$$\frac{\partial \omega}{\partial t} + U_j \frac{\partial \omega}{\partial x_j} = \alpha S^2 - \beta \omega^2 + \frac{\partial}{\partial x_j}\left[(\nu + \sigma_\omega \nu_T)\frac{\partial \omega}{\partial x_j}\right] + 2(1 - F_1)\sigma_\omega \frac{1}{\omega}\frac{\partial k}{\partial x_j}\frac{\partial \omega}{\partial x_j} \tag{22}$$

where

$$P_k = \tau_{ij}\frac{\partial u_i}{\partial x_j}, \tag{8}$$

$$\tau_{ij} = 2\mu_t S_{ij} - \frac{2}{3}\rho k \delta_{ij} \tag{9}$$

with τ_{ij} denoting the Reynolds stress (kgm^{-1}s^{-2}), S_{ij} the mean deformation rate component (s^{-1}), and δ_{ij} the Kronecker delta function.

$$F_1 = \tanh\left\{\min\left[\max\left(\frac{\sqrt{k}}{0.09\omega y}, \frac{500\mu}{\rho y^2 \omega}\right), \frac{4\rho\sigma_{\omega_2} k}{CDk_\omega y^2}\right]^4\right\}, \tag{10}$$

$$CD_{k\omega} = \max\left(2\rho\frac{1}{\sigma_\omega}\frac{\partial k}{\partial x_j}\frac{\partial \omega}{\partial x_j}, 10^{-10}\right), \tag{11}$$

$$\sigma_k = \frac{1}{F_1/\alpha_{k,1} + (1 - F_1)/\alpha_{k,\infty}}, \tag{12}$$

$$\sigma_\omega = \frac{1}{F_1/\alpha_{\omega,1} + (1 - F_1)/\alpha_{\omega,\infty}}, \tag{13}$$

α_k and α_ω are the turbulent Prandtl numbers for k and ω, respectively. μ_t (kg/ms) is the turbulence viscosity, which is calculated as follows:

$$\frac{1}{\rho}\mu_t = \frac{a_1 k}{\max(\alpha_\omega, SF_2)}, \tag{14}$$

$$F_2 = \tanh\left[\max\left(2\frac{\sqrt{k}}{0.09\omega y}, \frac{500\mu}{\rho y^2 \omega}\right)^2\right], \tag{15}$$

In Equation 14, the term $S = (2S_{ij}S_{ij})^{1/2}$ is an invariant measure of the strain rate, and $a_1 = 0.31$. The other constant values in the above equations are as follows:

$\beta^* = 0.09$,

$\sigma_{k,1} = 0.85, \quad \sigma_{k,2} = 1.0,$

$\sigma_{\omega,1} = 0.5, \quad \sigma_{\omega,2} = 0.856.$

Mesh and Boundary Conditions

The length and diameter of the pod are 30m and 4.5m respectively, similar to the hyperloop alpha design. The simulations were conducted by setting the moving zone speed, representing the pod velocity, to various values ranging from 100 $m\,s^{-1}$ to 350 $m\,s^{-1}$, including 150, 160, 170, 180, 190, 200, 210, 220, 230, 240, 250, and 300 $m\,s^{-1}$. To capture the drastic change in compressible flow behaviour around the pod between 150 $m\,s^{-1}$ and 250 $m\,s^{-1}$, the speed range was closely divided during this transition.

The Reynolds number was calculated using the background density and viscosity, pod speed, and hydraulic diameter of the gap between the tube and pod. Depending on the pod speed, the Reynolds number ranged from 13,000 to 45,500, indicating turbulent flow conditions. However, considering the high pod speed and large size, the Reynolds number was relatively low due to the minimal tube pressure.

A static pressure of 1/1000 atm was applied as the outlet pressure condition. The no-slip boundary condition was imposed on both the pod and tube walls, with the tube wall remaining stationary while the pod wall moved with the moving zone. The initial flow field conditions were set with a pressure of 1/1000 atm, a temperature of 300 K, and a zero velocity.

At the pod wall boundaries, wall functions are employed to reduce the cell count requirements compared to integrating all the way to the wall. This uses solution interpolations to predict the wall shear based on the local cell centroid values. The non-dimensional wall coordinates y+ are maintained between 30-300 to remain in the log-layer region where wall functions are valid.

The simulations were performed with no-slip boundary conditions applied on the pod's surface and the ground floor. The inflow turbulence intensity was set to 5%. All simulations were conducted in a transient mode, employing a time step of 0.1s, which was deemed appropriate to resolve any fluctuations in the aerodynamic forces acting on the system.

To solve the coupled system of governing equations, the Semi-Implicit Method for Pressure-Linked Equations (SIMPLE) algorithm was utilized. This algorithm, implemented in Simscale, employs the finite volume method for spatial discretization. Within each time step, multiple iterations were performed to ensure convergence of the solution.

The total simulation time was limited to 1 minute. Convergence was achieved within 80 iterations per time step, resulting in a total of 8,000 to 10,000 iterations over the entire simulation period.

4.1.4 Pod Exterior Analysis

4.1.5 Analysis of different aspects that affect performance

The next section analyses the results from a few previous studies that showed us how these factors interplay to affect pod performance in three distinct shapes. Each of the following subsections discusses aspects that affect pod performance and their relation the the pod's nose and tail shape.

Aerodynamic Drag and Blockage Ratio

In Jain A.(2019), it was analysed how different shapes of the head affect the drag under varying blockage ratios [14]. The analysis was performed on three distinct shapes; semicircle nose, arched-shaped nose, and splined elliptic nose. A rectangular tail (blunt tail) remains unchanged for each head shape, and the blockage ratio was varied between 0.25- 0.6. The pod travels at a speed of 0.3 M, and the pressure inside the tube is 860 Pa. Figure 21 shows the effect of head shape on the drag of the pod for various blockage ratios.

It was observed that an increase in blockage ratio caused a corresponding increase in drag [14]. Increasing the blockage ratio decreases the area available for the flow between the pod and the tube, thereby speeding up the fluid in the throat area [14]. This increase in the fluid velocity directly increases the drag. Secondly,

the shape of the head has no profound impact on the aerodynamic drag as it was approximately the same for blockage ratio ranging from 0.25 - 0.55 [14]. This could be attributed to the lower internal tube pressure [14]. However, at a blockage ratio of around 0.6, small effects begin to be observed because of the choking of the flow and formation of shock waves [14].

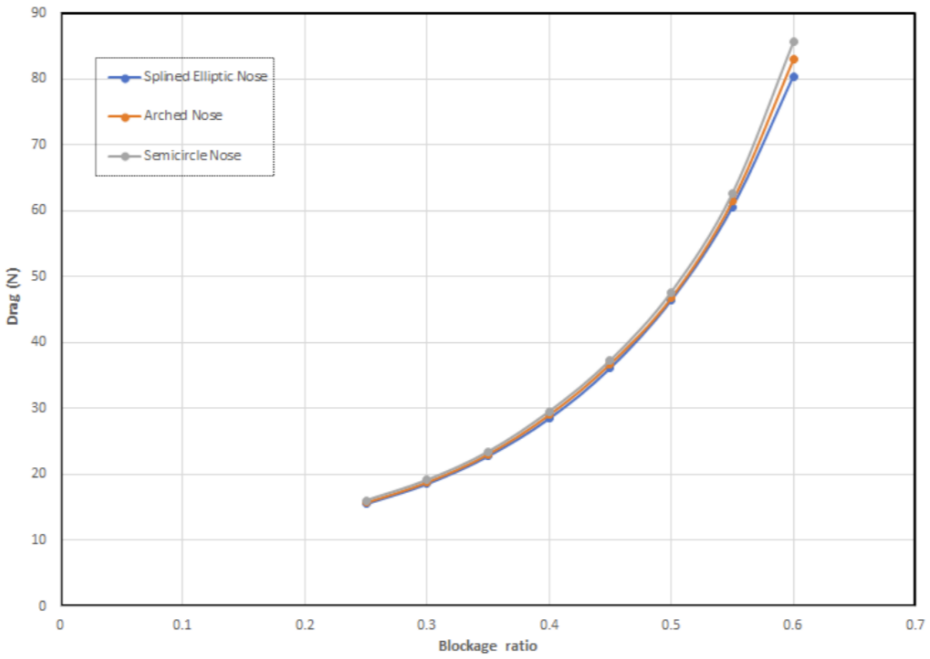

Figure 21: Effect of head shape on different B.Rs [14]

Furthermore, it was seen that when the pressure inside the tube ranges between 10 and 1000 Pa, the pod with a semicircle nose, arched nose and splined elliptic nose experiences almost the same amount of drag [14]. However, when this tube pressure exceeded 1 KPa, a gradual change in drag was observed which only became significant after 10 KPa [14]. Since the varying blockage ratio doesn't alter the tube pressure, which is below 1 KPa (860¡1000), no obvious effect of head shape on the aerodynamic drag is observed for varying blockage ratios as shown in the figure below [14].

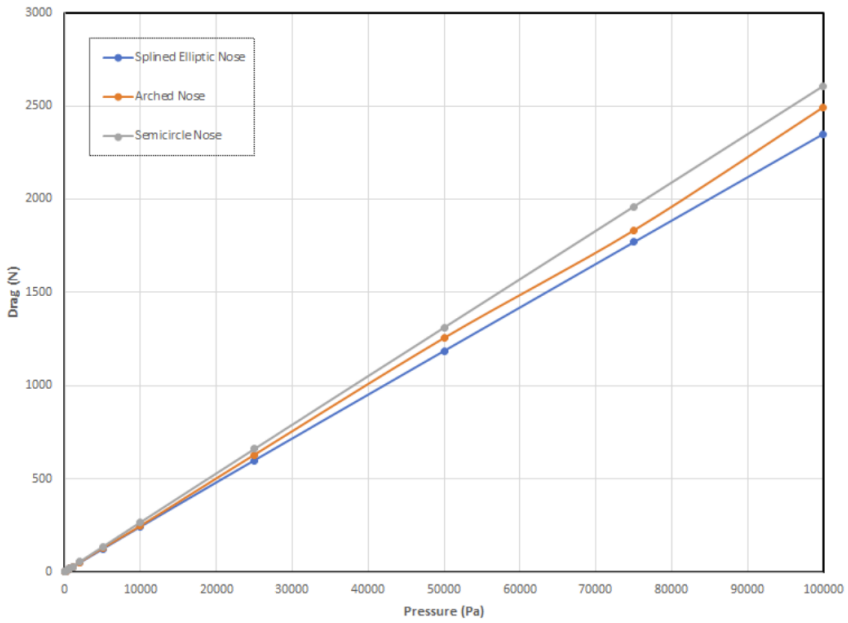

Figure 22: Effect of Head shapes on drag for different pressures [14]

Le et al. [8] performed a numerical analysis on pod shapes at different speeds and reached conclusions that gave us more insight. Drag increases along with an increase in speed [8].(Relevant results displayed in Figure 23).

The symmetrical design they chose has the lowest drag at all pod speeds, though this difference is only clearly observable at pod speeds higher than M_{cr}, or when choking occurs [8]. At a pod speed of 350 $m\,s^{-1}$, the difference between the reference case and when $N_U T_U$(The nose and tail of the pod are both upward and which has the highest drag) is 10.7%. The reference case uses an elongated pill shape with no particular inclination for the nose and tail direction [8].

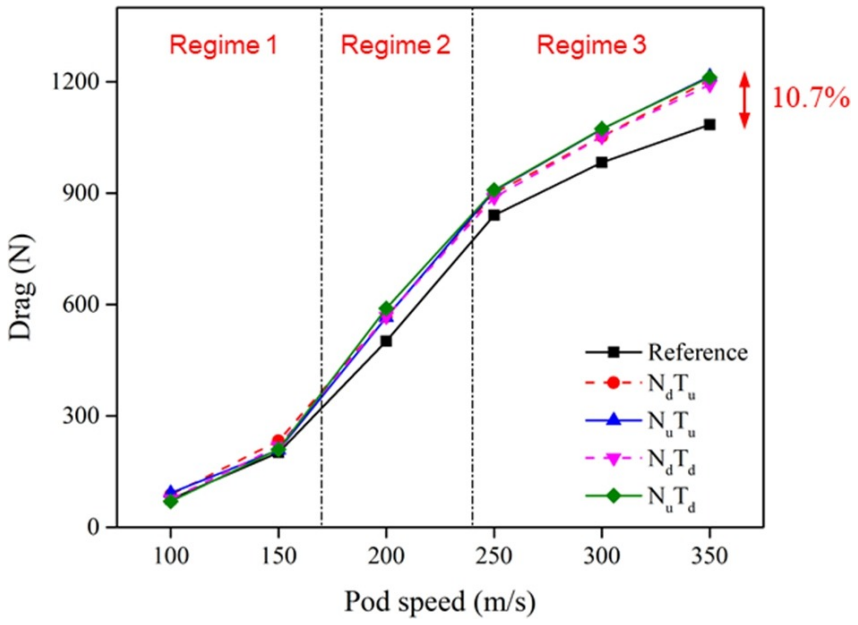

Figure 23: Drag acting on the pod for the five cases with respect to the pod speed and specified regimes[4]

Pressure Drag and Limiting Velocity

An important consideration for hyperloop systems is the pressure drag. This pressure drag emanates because of the pressure differential caused by the high-pressure region in front of the pod and the low-pressure wake. In other words, aerodynamic drag depends on the pressure distribution and the maximum pressure experienced. [14]

For a hyperloop pod travelling through an evacuated tube, the pressure drag dominates the viscous drag. Several studies, such as Kang et al. [60], have all reported that friction drag is responsible for less than 10% of overall aerodynamic drag. Many previous studies have shown that pressure drag is a major factor in the hyperloop system, while the contribution of friction drag is responsible for less than 10% of the overall drag [57, 60, 61].

For a specific tube pressure, there is an absolute velocity termed as the limiting velocity below which the head shape has no pronounced effect on the aerodynamic drag of the vehicle [14].

For example, when the pressure in the tube is 860 Pa, head shape does not affect velocity up to 100 $m\,s^{-1}$ and when this pressure reduces to 100 Pa, no effect is noticed for velocities up to 200 $m\,s^{-1}$ [14].

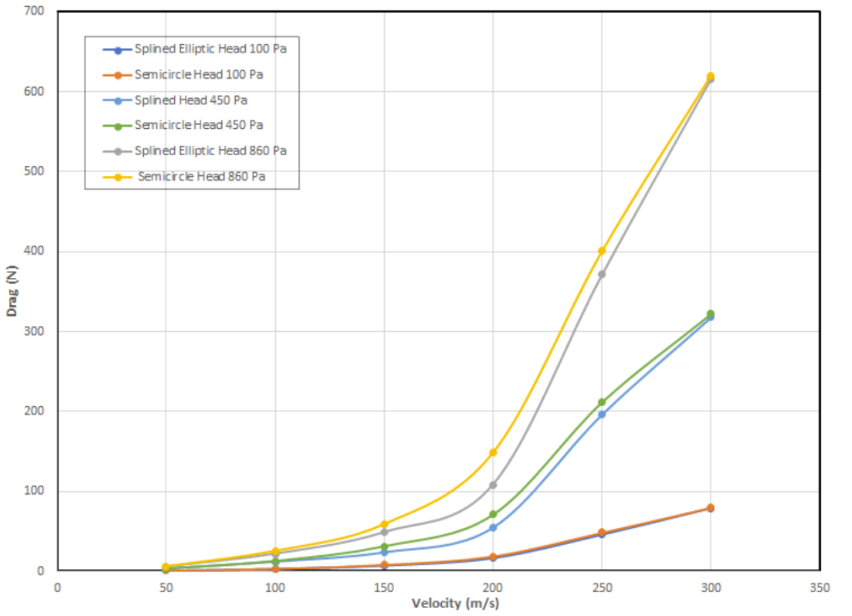

Figure 24: Total drag against the velocity for different head shapes and operating pressures [14]

This is because, for a given tail and head shape, the pressure drag is a function of the maximum pressure experienced by the nose of the pod [14]. Limiting Velocity is related to pressure drag since it's a function of the max pressure on the nose, the max total pressure is an algebraic sum of static and dynamic pressure so these pressures contribute to pressure drag.

When the pod travels at a relatively lower velocity ($< 200\,m\,s^{-1}$), the dynamic pressure is low [14]. Therefore according to the equation, the static pressure in the tube drives the total pressure [14].

For a given tail and head shape, the pressure drag depends on the maximum pressure at the nose of the pod, which is the sum of static and dynamic pressure. At lower velocities ($< 200\,m\,s^{-1}$), dynamic pressure is low, so static pressure in the tube primarily determines the total pressure. When this total pressure exceeds a critical value, the head shape impacts aerodynamic drag. Higher static pressure in the tube means less room for dynamic pressure before reaching the critical total pressure, making head-shape effects noticeable at lower velocities. At very high velocities, flow choking and shock formation can occur, raising total pressure regardless of tube static pressure. If total pressure surpasses the critical value, the head shape will influence aerodynamic drag. [14]

Pressure Difference and Lift

Pressure drag is calculated using:

$$F_{DP} = \Delta P \cdot A \tag{23}$$

where ΔP is the pressure difference between the nose and the tail of the pod, and A is the maximum cross-sectional area. The variation in drag is mostly affected by ΔP and is responsible for generating lift [8]. In the hyperloop system, aerodynamic lift is essential to help lift the pod along with the levitation of the magnetic field. Unlike drag, the shape of the nose and tail strongly affects the lift. [8]

Le et al. [8] observed how the lift of different pod shapes was affected at different pod speed regimes.

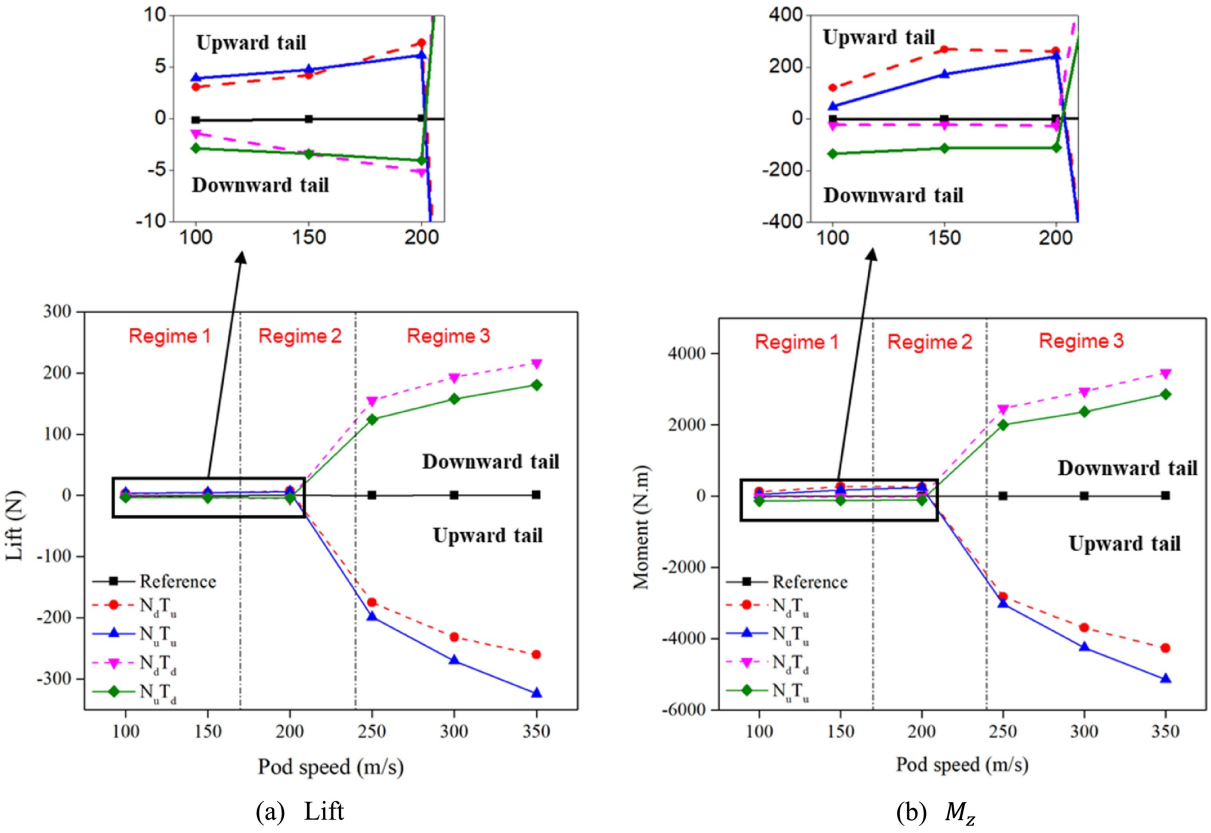

(a) Lift (b) M_z

Figure 25: (a) Lift acting on the pod for the five cases with respect to the pod speed. (b) Variation in the pitching moment (M_Z) with respect to the pod speed. [8]

The reference case was symmetric along both the x-y and x-z plans, therefore there was no lift due to the lack of ΔP between the upper and lower surfaces of the pod [8]. The variation in the pitching moment is also presented in Figure **??**(b).

Since the observed model is symmetric in the x–y plane; therefore, only the pitching moment is observed in the study. The differences in drag are low among all the 5 cases. Thus, the variation in the moment is similar to the variation in the lift [8]. Further analysis at different speed ranges reveals more to us about how different nose and tail variations affect lift. [8]

Analysis under different speed conditions

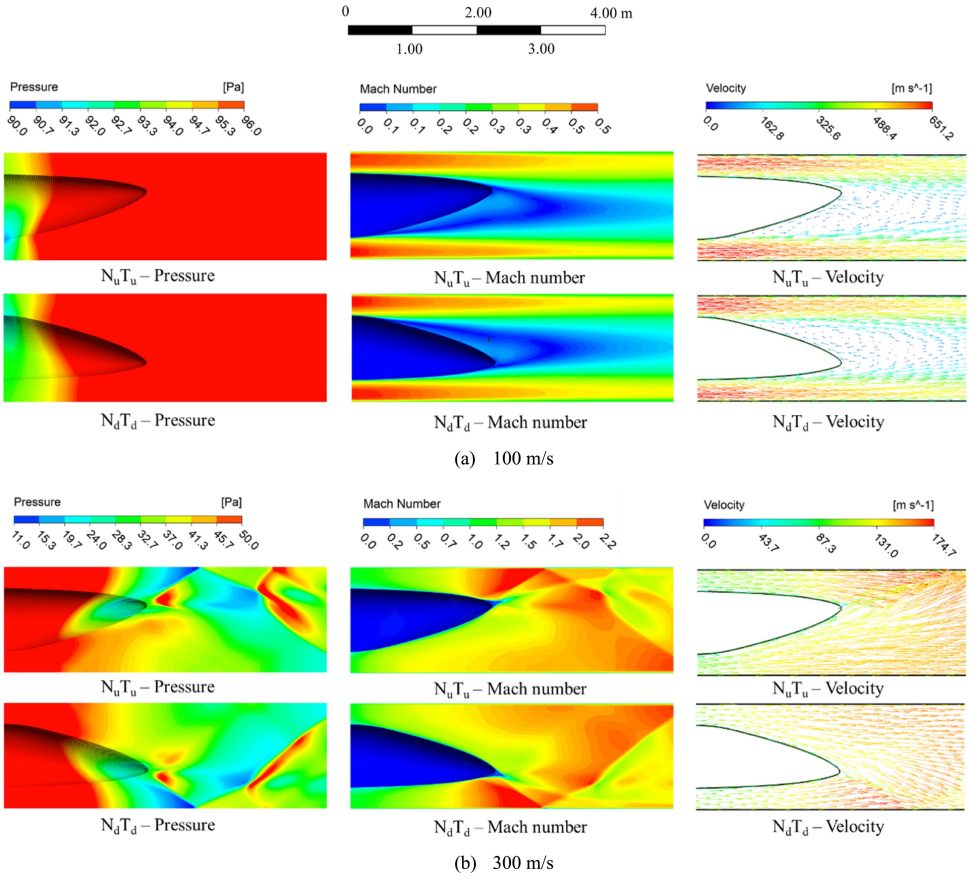

Figure 26: Side view of pressure contours, Mach number contours, and velocity vectors behind the pod for $N_U T_U$ and $N_D T_D$ at pod speeds of (a) 100 $m\,s^{-1}$ and (b) 300 $m\,s^{-1}$. [8]

Regimes 1 and 2 (pod speeds of 100 to 200 $m\,s^{-1}$)

In these two regimes, it was observed that a downward tail led to negative lift while an upward pod tail led to positive lift [8]. This is caused by the change in the area between the pod and the tube, moreover, the separation of the flow occurs at the end of the tail which causes velocity reduction and an increase in the pressure in the separation area. With an upward tail, the lower surface of the pod has a larger change in area compared with the upper surface. This results in a higher pressure on the lower surface, thus lifting the pod. On the other hand a downward tail, the opposite is observed, with a negative lift generated. However, the lift in these two regimes is comparatively very low when considering the third speed range.

Regime 3 (pod speeds of 200 to 400 $m\,s^{-1}$)

In speeds ranging from 250, 300, and 350 $m\,s^{-1}$, a reverse trend compared to Regimes 1 and 2 is noted. Here, an upward tail induces negative drag, while a downward tail results in positive drag [8]. This occurs since the fully accelerated flow in the divergent flow section of the pod, pushes an oblique shockwave behind the pod and increases the pressure differential between the pod's upper and lower surfaces [8]. Additionally, the tail design influences the pattern of the oblique shockwave, as illustrated in Figure 26(b).

To elucidate these findings, Figure 27 shows the average pressure on the upper and lower surfaces of the pod's nose and tail for both $N_U T_U$ and $N_U T_U$ pod shapes relative to pod speed [8]. The nose pressure remains unchanged, but the tail pressure showed significant variation in this case [8]. So it can be concluded that lift variation is heavily influenced by the tail shape. Notably, $N_U T_U$ and $N_D T_D$ exhibit opposite trends, as seen in Figures 27 and 28. [8]

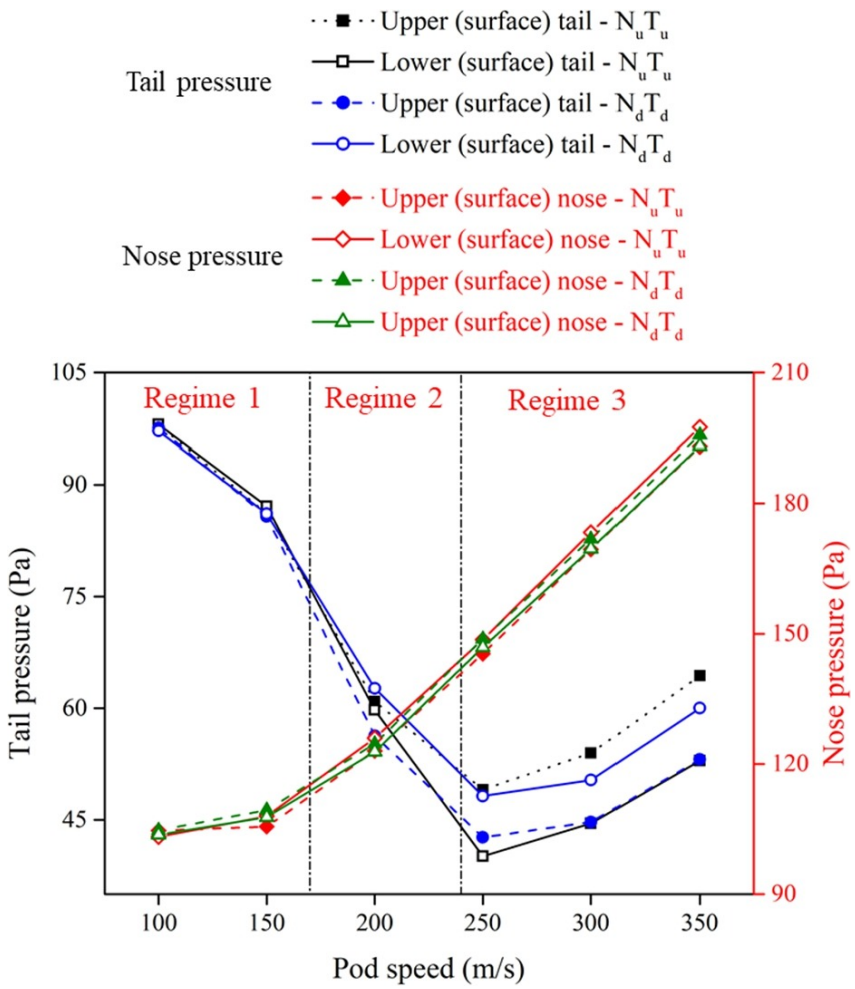

Figure 27: Pressure at the nose and tail of the pod for N_UT_U and N_DT_D with respect to the pod speed. [8]

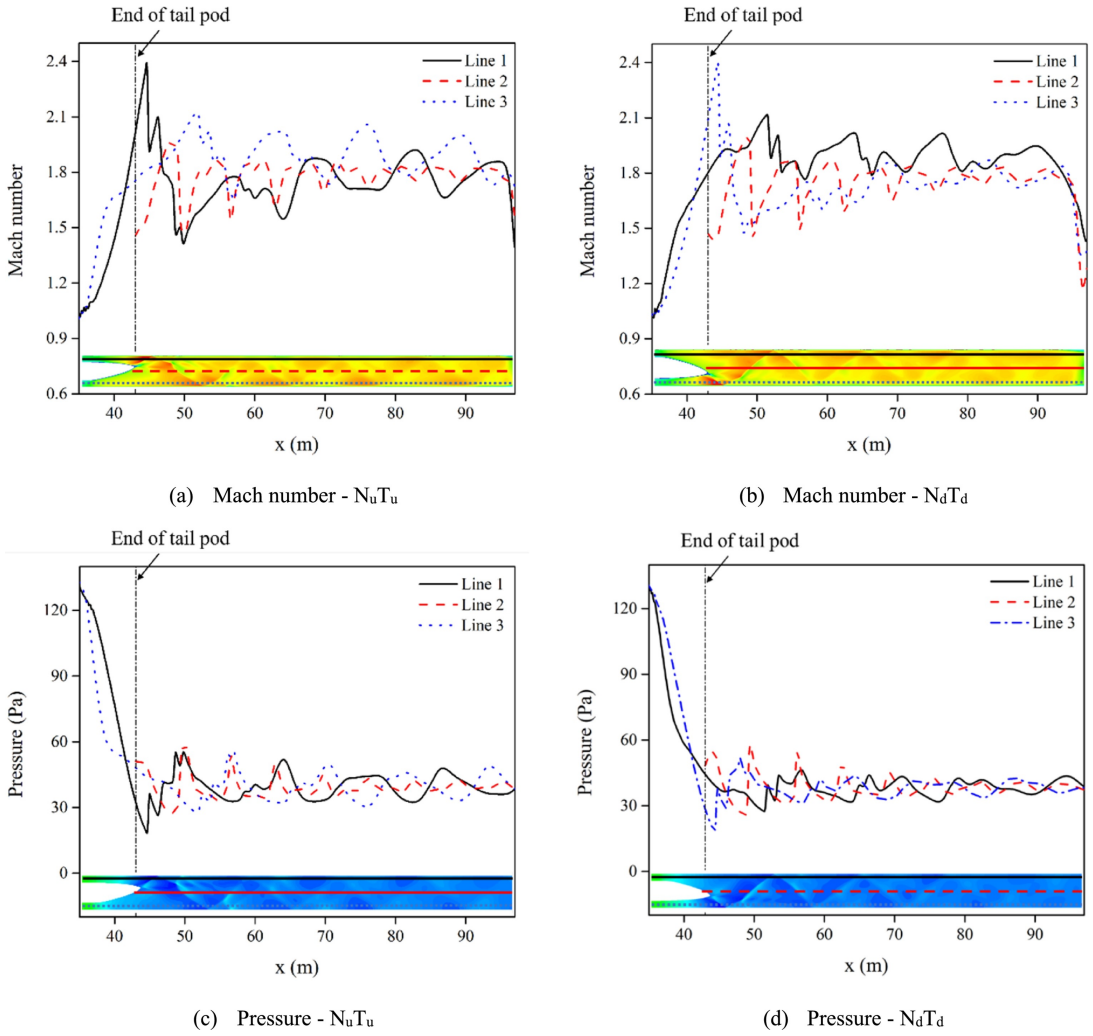

Figure 28: Mach number distribution and the pressure distribution behind the pod for $N_U T_U$ and $N_D T_D$, at a pod speed of 350 $m\,s^{-1}$. [8]

For the $N_D T_D$ configuration, featuring a downward tail, the pressure on the upper surface at the rear of the pod is lower than that on the lower surface, generating positive lift [8]. This is associated with local area changes during flow choking. [8]

As detailed earlier, in Regime 3, the flow fully accelerates in the divergent section. With a downward tail, the smaller area change below the pod causes the flow to gradually accelerate between the pod and the tube wall (see Figures 27(b) and 28(b)) [8]. Conversely, the local area above the pod increases rapidly, causing the local flow velocity to increase quickly, leading to lower pressures. [8]

At the tail's rear, the difference between the divergent section and the tube's total area is greater on the lower surface, resulting in the highest Mach number at the pod's lower rear end [8]. However, due to its location, this has a negligible impact on lift. [8]

Aerodynamic Lift Distribution

Another important consideration before the final conclusion is the lift distribution over the pod as it depends on the shape. As previously discussed, lift varies based on the pod's tail shape. Figure 29 compares the lift distribution between the front and rear halves of the pod (see Figure 30 for illustration) [8]. The pod's front half experiences significantly lower lift than the tail. For instance, at 350 $m\,s^{-1}$, $N_D T_D$ front lift constitutes only 4.6 % of the total lift [8]. For $N_U T_D$, despite the front lift being negative and the rear lift positive, the front lift's contribution is about 9 %, indicating that the lift on the front

half is considerably weaker than on the rear half. This underscores the tail shape's strong influence on lift variation. [8]

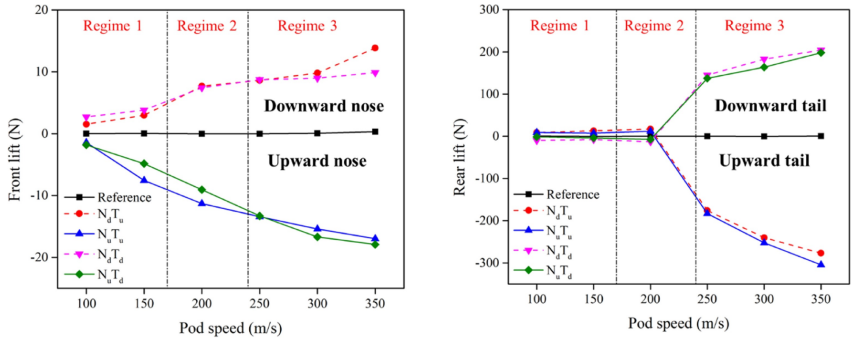

(a) Lift acting on front half (b) Lift acting on rear half

Figure 29: Lift acting on the (a) front and (b) rear halves of the pod. [8]

4.1.6 Pod design justification

The key findings from the studies were combined for use in the pod design:

1. Aerodynamic Drag: As displayed earlier The pod's nose or tail shape has minimal impact on drag except at certain speeds and pressures. The reference case shows a 10.7 % lower drag in Regime 3 (250 $m\,s^{-1}$ to 350 $m\,s^{-1}$) compared to other cases (N_DT_U, N_UT_U, N_DT_D, and N_DT_U), which exhibit similar drag levels. [8] The reference case uses an elongated pill shape with no particular inclination for the nose and tail direction. To use the advantages of life and maintain minimal drag, a nose and tail-down setup is recommended.

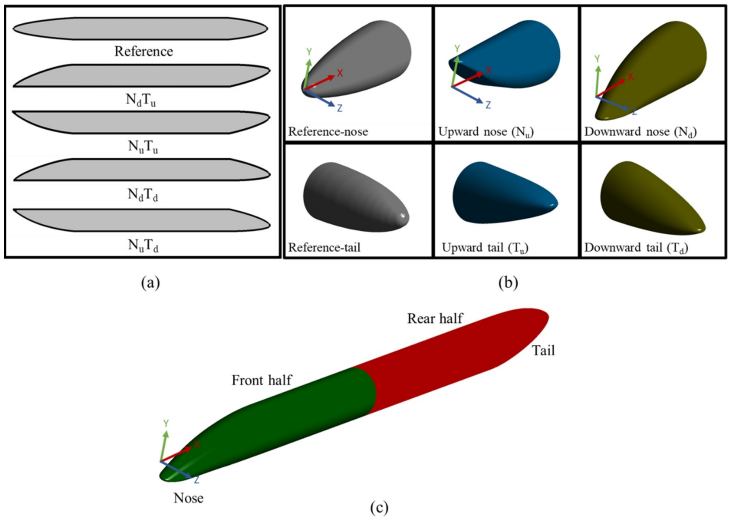

Figure 30: (a) Side views of the five cases.(b) Isometric view of the nose and tail for different pod shapes.(c) Isometric view of the geometry of N_DT_U. [8]

2. Aerodynamic Lift: Tail shape significantly affects lift. In Regimes 1 and 2, 100 $m\,s^{-1}$ to 200 $m\,s^{-1}$, an upward tail generates a positive lift, while a downward tail produces a negative lift [8]. In Regime 3, the opposite occurs: a downward tail generates a positive lift and an upward tail results in a negative lift [8]. Designing it according to the Regime 3 case, a nose and tail down setup is chosen for the design.

3. Lift Distribution: Total lift predominantly arises from the pod's tail, with less than 10 % attributable to the nose [8]. Interestingly, unlike the tail's lift variation across regimes, the front half of the pod

consistently shows a positive lift with an upward nose and a negative lift with a downward nose, regardless of the regime [8]. Taking this into consideration, it is again concluded that a downward tail would be the most suitable choice

4. Lift-to-Drag Ratio: This ratio increases with pod speed and a downward tail but decreases with an upward tail [8]. A higher ratio is more desirable since it implies a higher efficiency. The combined effect of all these factors would lead to an energy-efficient pod.

4.2 Materials

4.2.1 Aluminium Alloy

Due to its incredibly versatile nature, aluminium alloy is commonly used within the aerospace industry with alloy 2024 being the most prevalent [62]. With a density of roughly 2.7 $g\,cm^{-3}$, aluminium alloy is known for having a high strength-to-weight ratio, a key criterion for the hyperloop pod due to levitation weight dependence [63]. This feature is demonstrated in Figure **??** with the common aluminium alloys achieving much higher ratios than common steel alloys on average.

Table 10: Strength-to-Weight Ratio of Aluminium and Steel Alloys [23]

Class	Spec	Yield Strength (MPa)	UTS (MPa)	Strength-to-weight-ratio
Aluminium alloys	AA5182-O	125	270	0.9
	AA5754-O	110	220	0.7
	AA6111-T4	155	290	1.0
	AA6451-T4	110	210	0.7
	AA7075-T6	480	540	1.8
Steel grades	AKDQ	200	300	0.3
	HSLA 350	375	475	0.5
	DP 590	350	650	0.7
	DO 980	700	1050	1.2
	Press-hardened steel	1000	1500	1.7

Aluminium alloy typically has thermal conductivity values ranging from 90 to 150 $W\,m^{-1}\,K^{-1}$ [63]. Compared to other commonly proposed materials such as carbon fibre, with conductivity values forty times less, aluminium alloy contains unfavourable thermal properties for the hyperloop pod material which demands low conductivity due to the inability to remove heat from the system. Additionally, when exposed to air, aluminium alloy forms a protective oxide layer which contains anti-corrosive properties [64].

Aluminium alloy stands out as a hyperloop pod material due to being highly recyclable. To produce one tonne of new aluminium using the Bayer and Hall-Heroult processes, roughly 14000 kWh are required; conversely, it only requires 5% the amount of energy to obtain recycled alloy [62].

4.2.2 Polyetheretherketone

Polyetheretherketone (PEEK) plastics are incredibly strong and may be a viable material in the construction of the pod, thanks to its exceptional properties and versatility. In particular, it stands out as a high-performance plastic renowned for its resistance to heat and chemicals [15]. With durability comparable to metals, PEEK has one of the highest levels of heat resistance and mechanical strength among engineering plastics. Due to its crystalline structure, it has a high impact strength and it can withstand temperatures ranging from -50°C to +250°C and is self-extinguishing according to UL 94 VO, meaning that burning stops within 10 seconds [15, 65].

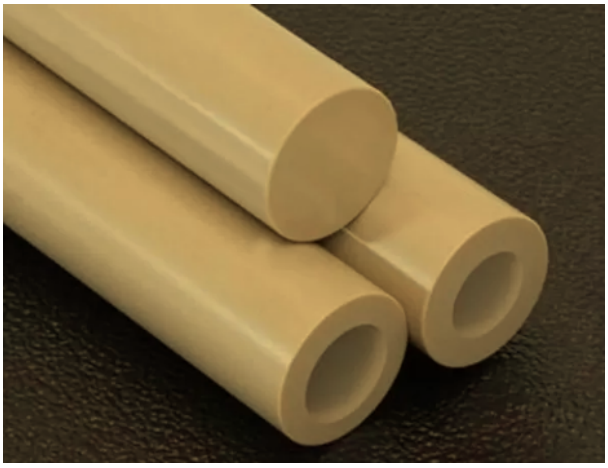

Figure 31: PEEK plastic [15]

The various types of PEEK, including glass-filled and carbon-filled variants, cater to diverse industrial needs. It has a place in the mechanical, electrical, and automotive industry, as well as the oil and gas industry. 30% carbon filled PEEK has a lower density than 30% glass filled PEEK, however, the carbon filled option still has a high mechanical strength value, and is often used in the automotive, electronics and aerospace fields [66]. In the realm of hyperloop pod construction, the material's impact resistance, heat resistance, and durability play pivotal roles. PEEK's remarkable ability to withstand extreme conditions while maintaining structural integrity ensures the safety and reliability of the hyperloop pods during high-speed travel. Additionally, it allows for the creation of intricate components essential for pod assembly. Additionally, PEEK plastic can be fully recycled by two methods: the plastic can be shredded and melted into new products or it can be broken down into its chemical components and those can be turned into new materials [67].

4.2.3 Polyaryletherketone

Polyaryletherketone (PAEK) plastics have a similar chemical structure to PEEK. The properties of PAEK fall between PEEK and other thermoplastics such as PEI (polyetherimide) and PAI (polyamide-imide) which are also very high-performing. For example, PAEK has a glass-transition temperature of 158°C, which is somewhat higher than that of PEEK, but significantly below that of PAI at 280°C [68]. Because it retains stiffness over 150°C, PAEK can be an alternative to PEEK for certain applications, depending on the stress load and the chemical environment. PAEK plastics have very few toxic and corrosive fumes and allow heat output when burned, increasing safety and meaning that it can also be an economical option to PEEK for applications that require high quantities of specific parts. PAEK resin is good for colourability, which can aid in the appearance of the pod [68].

Both PEEK and PAEK have good electrical insulation, which increases safety as they can withstand high voltages, as well as excellent corrosion resistance, which ensures the durability of the pod when exposed to rain or potentially corrosive substances, making it more reliable. Comparing PEEK and PAEK plastics to aluminium alloy, it is notable that these two plastics weigh considerably less, with both having a density of around 1.3 $mg\,m^{-3}$ [15, 69]. This can reduce costs as well as improve energy efficiency, as lighter pods would decrease the energy required to accelerate/decelerate. PEEK has a tensile strength of around 100 mPa while PAEK has a higher tensile strength of around 160 mPa, making it more durable [69]. Additionally, while both are recycled polymers, PEEK is fully recyclable while PAEK loses some quality when recycled [70, 71].

Figure 32: PAEK plastic [16]

4.2.4 Comparison of Materials

Table 11: Comparison of Aluminium Alloy, PEEK, and PAEK

Materials	Main advantages	Main disadvantages	Renewability
Aluminium Alloy	• Inherent anti-corrosion properties • Excellent strength-to-weight ratio compared to other metals	• Poor thermal conductivity values for a hyperloop • Lower strength-to-weight ratio than PEEK and PAEK	• Recycling aluminium alloy is significantly more energy efficient than acquiring new alloy
PEEK	• Self-extinguishing • Lightweight	• Weaker than aluminium alloy and PAEK	• Fully recyclable
PAEK	• Stronger than PEEK and many aluminium alloys • Lightweight • Low Toxicity	• Low glass-transition temperature	• Less easily recyclable than PEEK

Upon comparison, it is advised that PAEK be considered as the hyperloop pod material due to its high strength, exceptional conductivity values, and sustainability. A more detailed investigation of PAEK will need to be carried out before implementation. Particularly, a thermal analysis simulation will need to be run on a completed pod system to determine if any areas will reach temperatures above PAEK's transition temperature.

4.3 Interior Design

4.3.1 Analysis of CO2 Emission in the UK

In 2022, carbon dioxide (CO_2) emissions in the UK decreased by 2.2% [72]. Studies suggest that transportation sector is responsible for approximately 27% of the carbon emission in the UK [73]. In particular, domestic transport is known to be the largest contributor of CO_2 emission [74]. Moreover. resources also suggest that the 20 largest urban cities were responsible for 40% of the transport emission in the country [75]. Considering the impact of transportation, particularly between large urban cities, it is important to identify areas where CO_2 emission can be reduced within the transportation sector.

One of the busiest transportation routes in the United Kingdom connects the capital, London, to the Scottish capital of Edinburgh. With up to 45 trains [76] and over 10 flights (one-way) every day, this route can be considered a major contributor to the CO_2 emission as it connects two major cities in the country. An analysis of the Edinburgh-London route reveals that air travel contributes significantly to the overall carbon footprint [77]. The average CO2 emissions for a one-way flight on the route are approximately $155kg$ per passenger-kilometre. In comparison, rail travel on this route has a lower carbon emission of $22.42kg$ of CO_2 per passenger-kilometre on newer trains [77]. As seen in Figure 33, rail transportation has the lowest impact on the environment when compared to other modes of transport including road transport.

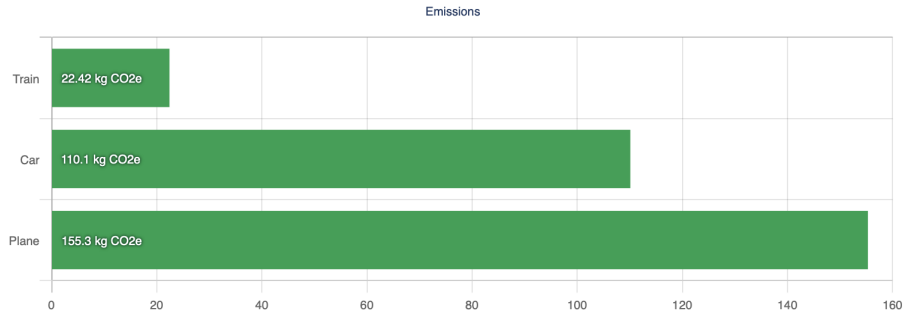

Figure 33: CO_2 Emission from different modes of transport on London to Edinburgh route [17]

Freight transportation also plays a significant role in carbon emission, with 8% of the global carbon emission being a result of freight transportation [78]. Transport statistics from the UK also provide evidence to suggest that carbon emission from freight transport has increased by 10% [79]. Similar to passenger transport, rail transport is one of the most environmentally friendly options for freight transport with lower carbon emissions [78]. Current research discusses the importance of cleaner transportation modes. Studies also discuss pathways to net zero emission for different modes of transport including rail and road [80].

One of the proposed solutions for reducing carbon emissions is based on the research done on hyperloop technology. Discussions in the literature state that faster modes of rail transport (like hyperloop) on shorter flight routes, like Edinburgh to London, can replace flight transportation while also providing the convince of faster travel [81]. While currently the designs proposed for hyperloop pods in the research primarily focus on transporting passengers, it is pivotal that research also considers using such technologies for freight transport, especially given the positive environmental impact of such a model of transport.

Currently, the designs of hyperloops primarily focus on transporting passengers. A design for the hyperloop with the ability to transport both passengers and freight in the same system could further optimise resource utilization and reduce emissions associated with separate modes of transportation. Hence, most hyperloop designs cater only to passenger transportation and not freight. Considering this gap in the literature, this study aims to provide a comprehensive overview of a pod interior that can be used for both people and freight transport.

4.3.2 Demand of Freight/Travel in Edinburgh-London

To understand the demand of travel in Edinburgh to London using hyperloop, theoretical capacity investigations are required to comprehend the actual transport capacity considering the realistic operational scenarios and safety constraints of the signalling system are taken into account [82]. Unfortunately, only a few studies exist regarding hyperloop capacity. In Hyperloop Alpha, it is reported that the pod will regularly depart every two minutes with the interdeparture time being decreased to 30 seconds during the peak hour [18].

Environment Journal stated that travelling by flight remained a number one choice for passengers looking to travel between London and Edinburgh (400 miles journey) in 2019 [76]. At this time, rail only accounted for just one-third of all trips. However, in 2022, the situation changed significantly when 545 of the journeys on the route were taken via train.

On the other hand, Global Railway Review reported in one of their articles that research conducted by sustainability transport charity Transform Scotland has found that there is an increment in both air and rail travel between Scotland's Central Belt and London. Despite this, carbon emissions are still falling because more people are choosing train [83].

In another article published by The Independent, a transportation expert has disclosed that over half of travellers journeying from London to Edinburgh are now choosing to travel by train. According to recent data from RAIL, a transport magazine managed by Nigel Harris, there has been a rise of more than a third in the number of rail journeys between these two cities over the past year. Specifically, from April to August 2022, 57% of travellers opted for the train instead of flying [84]

Based on the reports published in these articles, it can be concluded that the demand to travel by train for the Edinburgh-London journey has significantly increased compared to air travel.

4.3.3 Key Criteria of Interior Design

The key criteria for the interior design of the pod must be carefully determined to ensure that the intended functionality is met and that a positive user experience is provided.

One of the primary requirements for the interior design is that the physical aspects of the pod's interior must be created to avoid causing claustrophobia among travelers, as they will be in an enclosed space for the duration of the journey. Claustrophobia is an intense fear of confined or enclosed spaces that can cause significant discomfort or panic in those affected. Since passengers will be inside the pod for the entire trip, it's crucial to design the space to feel open and comfortable, avoiding a cramped and restrictive environment. One of the strategies that can be employed is having a spatial layout that provides enough space for passengers to move around and stretch out, which can help mitigate feelings of confinement. This could include wider seats, higher ceilings, and more legroom [85].

Next, the safety and comfort of potential customers should also be prioritized when designing the interior of the pod. Traveling through a vacuum can introduce various sources of discomfort. One significant issue is the excessive noise from high-speed travel, necessitating careful attention to the capsule propulsion system. This noise comes from the vibration of the capsule, suspension system, or motors. In addition to this, pressure changes, which are often felt in the ears, can cause additional discomfort for passengers traveling in the pod [85].

Regarding safety measures, the pod's interior design must address ways to prevent accidents or injuries to passengers. This involves designing adequately wide aisles for passage and ensuring proper seat belt design for high-speed travel. Effective communication of safety procedures to passengers is also crucial. In addition to this, interior design must incorporate an emergency evacuation plan to ensure safe escape during unexpected events, such as a fire. A stabilisation cabin pressure system is necessary to handle depressurisation, with the capability to deploy oxygen masks and supply additional air from stored tanks [85].

The interior environment of the pod must also be considered when optimising the best interior design. Key elements to monitor include air conditioning, ventilation, and illumination. Inadequate measures

in these areas can cause passenger discomfort due to unpleasant air temperature and air velocity within the enclosed space. Therefore, air quality must be meticulously controlled throughout the design and operation process [85].

4.3.4 How to Optimise Seating and Passenger Flow

Optimisation of the appropriate design of the passenger seating is crucial to create an impression of space and ensuring passenger's comfort. As discussed in the previous section, this impression of space is important to tackle the claustrophobia issue due to the travelling in the confined space.

According to Elon Musk, the appropriate seating is proposed to be 2 X 14 seats [18]. The Hyperloop passenger subcapsule notional location is as illustrated below:

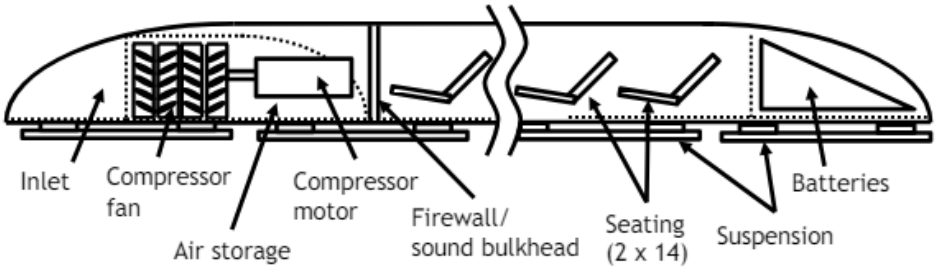

Figure 34: The Hyperloop Passenger Subcapsule Notional Location [18]

This overall interior weight is expected to be around 2500 kg. This include seats, restraint systems, interior and door panels, luggage compartment and entertainment displays. The interior components cost are targeted not to exceed $255,000 [18].

Classes of Capacity

To optimise the seating and passenger flow, there are three possible options of the interior designs that can be analysed. The seating can be classified into 3 classes of capacity which are: low-capacity (28 seats), medium-capacity capsule (40 seats), and high-capacity capsules (50 seats) [19].

Low-capacity capsule

The first possible layout of the Hyperloop capsule is a low-capacity capsule. The details of the design are as summarised in the table below:

Table 12: Characteristics of low-capacity capsule [19]

Parameter	Values
Number of seats	28
Overall length (m)	19.76
Frontal length (m)	8.96
End of capsules length (m)	1.82
Spaces between seats (m)	8.98
Maximum width of capsule (m)	3.06

The proposed layout is shown in figure below:

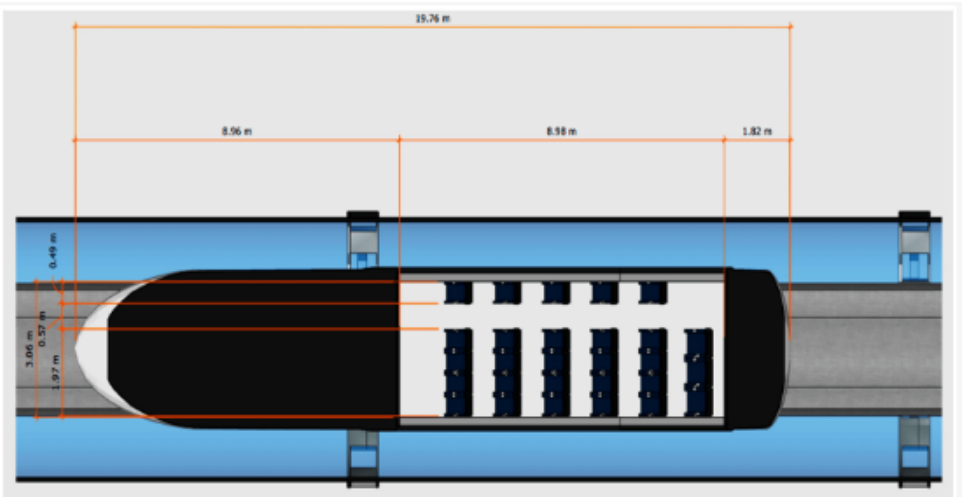

Figure 35: Low Capacity Capsule (Top View) [19]

This low-capacity capsule is designed with a rounded corner with no inclusion of any components of propulsion or suspension.

Medium-capacity capsule

Next, the second possible layout of the hyperloop capsule is a medium-capacity capsule. The details of the design are summarised in the table below:

Table 13: Characteristics of medium-capacity capsule [19]

Parameter	Values
Number of seats	40
Overall length (m)	22.48
Frontal length (m)	8.95
End of capsules length (m)	1.82
Spaces between seats (m)	11.96
Maximum width of capsule (m)	2.54

The proposed layout is as shown in figure below:

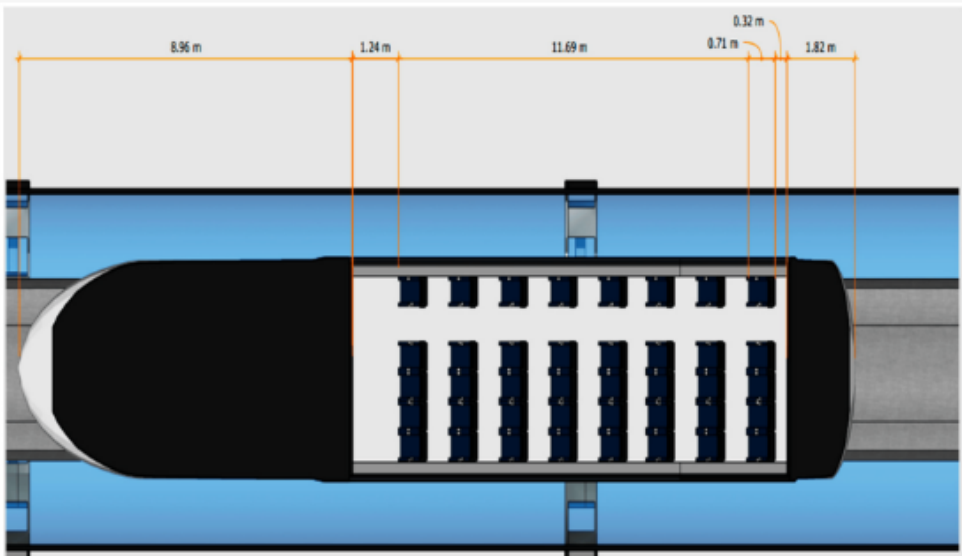

Figure 36: Medium Capacity Capsule (Top View) [19]

_High-capacity capsule

Lastly, the third possible layout of the Hyperloop capsule is a high-capacity capsule. The details of the design are as summarised in the table below:

Table 14: Characteristics of high -capacity capsule [19]

Parameter	Values
Number of seats	50
Overall length (m)	25.01
Frontal length (m)	8.96
End of capsules length (m)	1.82
Spaces between seats (m)	14.23

The proposed layout is as shown in figure below:

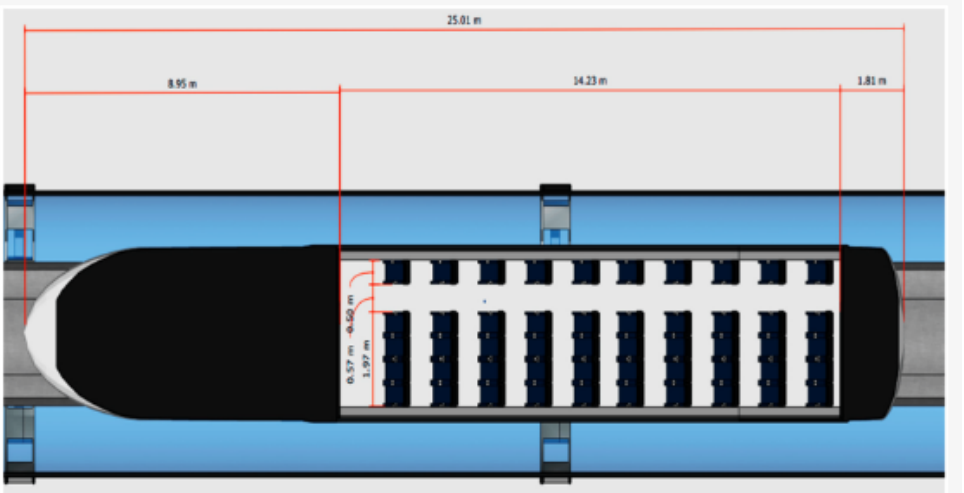

Figure 37: High Capacity Capsule (Top View) [19]

4.3.5 Discussion and analysis of the sustainability of the different capsule length

It can be observed from the previous section that the greater the capacity the capsule can hold, the longer its length will be.

Low-capacity capsule exhibit the shortest capsule length. Shorter capsules typically consume less energy per trip due to their lower mass, making them more energy-efficient for frequent, shorter routes. However, they may require more trips to transport the same number of passengers or goods, which can offset the initial energy savings. In terms of capacity and demand management, they can be more easily scaled to match fluctuating demand, reducing the risk of running under-utilised services. However, lower capacity per trip may not be sufficient during peak times, requiring more capsules or more frequent trips, potentially increasing energy consumption and wear on infrastructure.

On the other hand, high-capacity capsule can be more energy-efficient per passenger or ton of freight due to economies of scale although the initial energy required to start and stop longer capsules is higher, which can be a drawback for routes with frequent stops. In terms of capacity and demand management, higher capacity per trip makes longer capsules ideal for high-demand routes, reducing the need for frequent services and thus conserving energy. However, they are less flexible in adjusting to sudden drops in demand, potentially leading to under-utilisation and inefficiencies.

Discussing in term of sustainability, shorter capsules may produce typically lower emissions per trip but may require more trips, potentially increasing overall emissions. Longer capsules has higher emissions per trip but fewer trips needed, potentially lowering overall emissions when demand is high. Shorter capsules also potentially have lower initial costs and are better for variable demand scenarios but may incur higher operational costs due to frequent services. In contrast, longer capsules have higher initial infrastructure costs but are more cost-effective on busy routes with consistent high demand.

To conclude, the sustainability of capsule length is context-dependent. Shorter capsules offer flexibility and lower initial costs, making them suitable for urban and variable-demand scenarios. In contrast, longer capsules provide efficiency and capacity for high-demand, long-distance routes but require significant infrastructure investment. Balancing these factors is key to developing a sustainable hyperloop system that meets diverse transportation needs while minimizing environmental impact and ensuring economic viability.

5 Conclusion

After the investigation of cryopumps, turbomolecular pumps, and dry screw pumps regarding their feasibility in a hyperloop system, it was determined the most optimal pairing will be a turbomolecular pump with a dry screw forepump. This combination allows for high vacuum strengths to be reached while maximising energy efficiency and reducing maintenance. Using the energy consumption of the turbomolecular pump, combined with the drag reduction of a compressor implemented into a pod, it was determined that the optimal tube pressure for a pod travelling at $0.8\,M$ in a concrete tube is between 500 and $1000\,Pa$. The egressing air from the compressor was investigated and the most optimal usage was determined to be propulsion as air bearings are unstable and increase safety risk. The propulsion provided by egressing air was not considered in the calculation of optimal tube pressure and remains an area of further research. However, as the egressing air will combat drag, considering the propulsion benefits is expected to increase the optimal tube pressure.

In order to maximise lift and minimise drag, it was determined that a nose-and-tail down configuration be implemented into the pod design. The length of the pod will be determined on a case-by-case basis, dependent on the length of travel between destinations. Finally, it is recommended that PAEK be considered as the construction material for the pod due to its high strength-to-weight ratio, favourable conductivity properties, and sustainability. A full analysis of PAEK's suitability in a hyperloop system is yet to be conducted.

References

[1] M. A. S. Mahmood, Y. V. Rodionov, N. D. Vyacheslavovich, V. N. Vladimirovich, and D. N. Protasov, "A Comprehensive Review of Liquid Ring Vacuum Pumps and Compressors for Improving Global Efficiency and Energy Saving," *AIUB JOURNAL OF SCIENCE AND ENGINEERING*, vol. 21, no. 1, Jan. 2022.

[2] H. Bangcheng, Z. He, X. Zhang, X. Liu, T. Wen, and S. Zheng, "Loss estimation, thermal analysis, and measurement of a large-scale turbomolecular pump with active magnetic bearings," *The Institution of Engineering and Technology*, vol. 14, no. 7, pp. 1283–1290, Jul. 2020.

[3] "Eddy Current Drives Aid Centrifugal Pumps in Controlling Flow and Pressure | Pumps & Systems," Apr. 2019. [Online]. Available: https://www.pumpsandsystems.com/eddy-current-drives-aid-centrifugal-pumps-controlling-flow-and-pressure

[4] C. Day, "Basics and applications of cryopumps," pp. 241–274, Jan. 2007, mAG ID: 1561957669 S2ID: 2fceb110c0e454adf280e47167351d47f6ab06ae.

[5] "Dry Screw Vacuum Pump Working Principle," 2024. [Online]. Available: https://www.nashpumps.com/en-us/technologies-by-nash/dry-screw-vacuum-pump-technology

[6] V. A. International, "Dry Pumps: Screw Type," Dec. 2019. [Online]. Available: https://vacaero.com/information-resources/vacuum-pump-technology-education-and-training/191960-dry-pumps-screw-type.html#:~:text=Phase%201%3A%20Gas%20enters%20inlet,separated%20from%20the%20pump%20inlet.

[7] Maurice Bizzozero, Y. Sato, and Mohamed Aly Sayed, "Aerodynamic study of a Hyperloop pod equipped with compressor to overcome the Kantrowitz limit," *Journal of Wind Engineering and Industrial Aerodynamics*, vol. 218, p. 104784, Nov. 2021, mAG ID: 3201823247 S2ID: 5588d05f1156441745acf06bc83d2b8cb54bee05.

[8] T. T. G. Le, J. Kim, K. S. Jang, K.-S. Lee, and J. Ryu, "Numerical study on the influence of the nose and tail shape on the aerodynamic characteristics of a Hyperloop pod," *Aerospace Science and Technology*, vol. 121, p. 107362, Feb. 2022. [Online]. Available: https://www.sciencedirect.com/science/article/pii/S1270963822000360

[9] "Aeroheating and aerodynamic performance of a transonic hyperloop pod with radial gap and axial channel: A contrastive study," *Journal of Wind Engineering and Industrial Aerodynamics*, vol. 212, p. 104591, May 2021, publisher: Elsevier. [Online]. Available: https://www.sciencedirect.com/science/article/pii/S0167610521000775

[10] J. Galindo, V. Dolz, R. Navarro, B. Pallás, and G. Torres, "Methodology for a Numerical Multidimensional Optimization of a Mixer Coupled to a Compressor for Its Integrationin a Hyperloop Vehicle," *Applied Sciences*, vol. 12, no. 24, p. 12795, Jan. 2022, number: 24 Publisher: Multidisciplinary Digital Publishing Institute. [Online]. Available: https://www.mdpi.com/2076-3417/12/24/12795

[11] F. Lluesma-Rodríguez, T. González, and S. Hoyas, "CFD Simulation of a Hyperloop Capsule Inside a Low-Pressure Environment Using an Aerodynamic Compressor as Propulsion and Drag Reduction Method," *Applied Sciences*, vol. 11, no. 9, p. 3934, Jan. 2021, number: 9 Publisher: Multidisciplinary Digital Publishing Institute. [Online]. Available: https://www.mdpi.com/2076-3417/11/9/3934

[12] E. Chaidez, S. P. Bhattacharyya, and A. N. Karpetis, "Levitation Methods for Use in the Hyperloop High-Speed Transportation System," *Energies*, vol. 12, no. 21, p. 4190, Nov. 2019. [Online]. Available: https://www.mdpi.com/1996-1073/12/21/4190

[13] Y. Rana, "On the Feasibility of the Hyperloop Concept," May 2020. [Online]. Available: https://dspace.mit.edu/bitstream/handle/1721.1/127876/1196833048-MIT.pdf

[14] A. Jain, "STUDY OF THE EFFECT OF SHAPE ON THE AERODYNAMIC PERFORMANCE OF HYPERLOOP POD," Ph.D. dissertation, University of Florida, Dec. 2019. [Online]. Available: https://ufdcimages.uflib.ufl.edu/UF/E0/05/60/36/00001/Jain_A.pdf

[15] "PEEK Plastic." [Online]. Available: https://www.peekchina.com/peek-pipe/peek-plastic.html

[16] 3Devo, "Testing PAEK - Is It Any Good?" Jul. 2017. [Online]. Available: https://www.3devo.com/blog/testing-paek-is-it-any-good

[17] "Carbon Calculator," publication Title: ScotRail. [Online]. Available: https://www.scotrail.co.uk/carbon-calculator

[18] E. Musk, "Hyperloop Alpha," *SpaceX*, 2013.

[19] H. Almujibah, "Assessing Hyperloop Transport Optimizing Cost with Different Designs of Capsule," *Processes*, vol. 11, no. 3, p. 744, Mar. 2023, number: 3 Publisher: Multidisciplinary Digital Publishing Institute. [Online]. Available: https://www.mdpi.com/2227-9717/11/3/744

[20] Jiho Park, Junseok Ko, Hyobong Kim, Sangyoon Chu, Jongwoo Kim, Juwon Kim, Sehwan In, Yongju Hong, Seongje Park, and Hankil Yeom, "Development of a large capacity cryopump equipped with a two-stage GM cryocooler," *Applied Thermal Engineering*, pp. 119 217–119 217, Aug. 2022, mAG ID: 4293329430 S2ID: 48659813b70db9b751597c743b49b822aaebc344.

[21] Y. Murayama, H. Shikano, H. Endo, T. Harayama, and K. Takahashi, "22-inch Cryopump that Achieves Both Cost reduction and Energy Saving," *The Technical Journal*, vol. 85, pp. 35–41, Jun. 2023. [Online]. Available: https://www.ulvac.co.jp/en/research_development/technical_journal/85E/TJ85E_6.pdf

[22] J. Kim, K. S. Jang, T. G. Le, K. Lee, and J. Ryu, "Theoretical and numerical analysis of pressure waves and aerodynamic characteristics in Hyperloop system under cracked-tube conditions," *Aerospace Science and Technology*, pp. 107 458–107 458, Mar. 2022, mAG ID: 4214863220 S2ID: cf91095b250f4101372703c5e67368dcff47d00e.

[23] T. Feister, H. Kim, A. Gwinn, T. Schiller, and M. Austin, "Failure predictions in warm forming of 7075-T6 aluminum structural parts," *IOP Conference Series: Materials Science and Engineering*, vol. 418, p. 012024, Sep. 2018. [Online]. Available: https://iopscience.iop.org/article/10.1088/1757-899X/418/1/012024

[24] J. Kim, T. G. Le, M. Cho, and J. Ryu, "Theoretical and numerical analysis of effects of sudden expansion and contraction on compressible flow phenomena in Hyperloop system," *Aerospace Science and Technology*, pp. 107 587–107 587, Apr. 2022, mAG ID: 4225157678 S2ID: c16acb948c3943a6632440dd84ae7f08fe38ffee.

[25] F. Alcántara-Ávila, F. Lluesma-Rodríguez, T. Gonzalez, T. González, and S. Hoyas, "CFD Simulation of a Hyperloop Capsule Inside a Low-Pressure Environment Using an Aerodynamic Compressor as Propulsion and Drag Reduction Method," *Applied Sciences*, vol. 11, no. 9, p. 3934, Apr. 2021, mAG ID: 3158661967 S2ID: 5b9e3fd8388c13684f83a92acf2a3deabe18295d.

[26] "Introduction to Air Bearings." [Online]. Available: https://www.specialtycomponents.com/Resources/Technical-Articles/Introduction-to-Air-Bearings/#:~:text=Air%20bearings%20fall%20into%20two,their%20own%20internal%20pressure%20differentials

[27] M. Heldner, M. Heldner, H.-P. Kabelitz, and H. Kabelitz, "Reliability of turbomolecular vacuum pumps: A comparison of rolling element and magnetic bearing systems," *Journal of Vacuum Science and Technology*, vol. 8, no. 3, pp. 2772–2777, May 1990, mAG ID: 2160568773 S2ID: c4b9faec73cfd1d02f9f7a9750a275ef14ee9ccf.

[28] Fausto Casaro and F. Casaro, "Vibrations in turbomolecular pumps: Spectra and source location," *Journal of Vacuum Science and Technology*, vol. 7, no. 3, pp. 2377–2380, May 1989, mAG ID: 1967588425 S2ID: 578413d1c944e5270ac18380ecb2abaa99e02cdf.

[29] N. Ogiwara, K. Kanazawa, T. Inohara, and K. Wada, "Influence of magnetic fields on turbo-molecular pumps," *Vacuum*, vol. 84, no. 5, pp. 718–722, Dec. 2009. [Online]. Available: https://www.sciencedirect.com/science/article/pii/S0042207X09003364

[30] Yoshiki Murakami, Y. Murakami, Tetsuya Abe, T. Abe, T. Abe, Shigeki Morii, S. Morii, N. Nakaishi, N. Nakaishi, Satoshi Hata, and S. Hata, "Performance test of a ceramic rotor developed for turbomolecular pumps for fusion use," *Journal of Vacuum Science and Technology*, vol. 5, no. 4, pp. 2599–2602, Jul. 1987, mAG ID: 1994382545 S2ID: d08dd062075ba9bcd70ef065c97314bc267fe98f.

[31] Ziyuan Huang, Z. Huang, Bangcheng Han, B. Han, B. Han, Kun Mao, K. Mao, T. Chongjian, Cong Peng, C. Peng, Cong Peng, Jiancheng Fang, and J. Fang, "Mechanical stress and thermal aspects of the rotor assembly for turbomolecular pumps," *Vacuum*, vol. 129, pp. 55–62, Jul. 2016, mAG ID: 2319770146 S2ID: d27bf1b9b902e4efb8d233da5731cd8a2459ca8b.

[32] "Excerpt from the Oerlikon Leybold Vacuum Full Line Catalog 2015/2016 Catalog Part High Vacuum Pumps," 2016.

[33] "Turbomolecular pumps what you need to know," Nov. 2020. [Online]. Available: https://www.leybold.com/en-uk/knowledge/blog/turbomolecular-pumps-what-you-need-to-know#:~:text=Turbomolecular%20pumps%20offer%20a%20reliable,s%20to%203000%20l%2Fs.

[34] Y. Iwasa and S. Ito, "A new type of cryopump with a metal cryopanel cooled below 3.6 K by a two-stage GM refrigerator," *Vacuum*, vol. 47, pp. 675–678, Jun. 1996, mAG ID: 2021658919.

[35] X. Hao, S. Yao, and T. Schilling, "Design and experimental investigation of the high efficiency 1.5 W/4.2 K pneumatic-drive G-M cryocooler," *Cryogenics*, vol. 70, pp. 28–33, Sep. 2015, mAG ID: 2025082266.

[36] R. Gangradey, J. S. Mishra, S. Mukherjee, P. Nayak, P. Panchal, J. Agarwal, and V. Gupta, "Experimental Investigation of Thermal Properties of Materials Used to Develop Cryopump," *Fusion Science and Technology*, vol. 77, no. 5, pp. 333–339, May 2021, mAG ID: 3160998666 S2ID: 2fc5897813ad6c499dec1dfad7a303c49207a0ce.

[37] M. B. Kravchenko and G. K. Lavrenchenko, "Improving the Efficiency of a Gifford–Mcmahon Cryogenic Refrigerator," *Chemical and Petroleum Engineering*, vol. 55, no. 5, pp. 392–401, Sep. 2019, mAG ID: 2979309301.

[38] Ranjana Gangradey, Samiran S. Mukherjee, Vishal Gupta, Paresh Panchal, Pratik Nayak, Jyoti S. Mishra, Avijit Dewasi, and Shashi Kant Verma, "Design and development of a liquid nitrogen cooled test cryopump for application in steady-state superconducting Tokamak-1," *Vacuum*, pp. 110 986–110 986, Mar. 2022, mAG ID: 4221094894 S2ID: 4cd4277c93d93a525aa42169a90a4c5771f35056.

[39] S. Mukherjee, P. Panchal, P. Nayak, V. Gupta, V. Gupta, V. Gupta, S. Das, J. S. Mishra, R. Gangradey, R. Gangradey, and R. Gangradey, "Nitrogen and water vapor pumping study on a 400 mm opening LN2 cooled sorption cryopump," *Vacuum*, vol. 184, p. 109883, 2020, mAG ID: 3096131674.

[40] "EDS Dry Screw Vacuum Pumps." [Online]. Available: https://www.edwardsvacuum.com/en-in/vacuum-pumps/our-products/dry-screw-pumps/eds#tabs-v2-0efdf35dd1-item-e36fb36153-tab

[41] "Everything you need to know about screw pumps," Nov. 2019. [Online]. Available: https://www.leybold.com/en-uk/knowledge/blog/working-with-screw-pumps

[42] "Fixed speed dry screw vacuum pumps." [Online]. Available: https://vacaero.com/information-resources/vacuum-pump-technology-education-and-training/191960-dry-pumps-screw-type.html#:~:text=Phase%201%3A%20Gas%20enters%20inlet,separated%20from%20the%20pump%20inlet.

[43] M. H. Hablanian, "The emerging technologies of oil-free vacuum pumps," *Journal of Vacuum Science & Technology A: Vacuum, Surfaces, and Films*, vol. 6, no. 3, pp. 1177–1182, May 1988. [Online]. Available: https://pubs.aip.org/jva/article/6/3/1177/100048/The-emerging-technologies-of-oil-free-vacuum

[44] A. Tengler, "The benefits of oil-free vacuum pumps in industrial processes," *World Pumps*, vol. 2005, no. 460, pp. 18–21, Jan. 2005. [Online]. Available: https://linkinghub.elsevier.com/retrieve/pii/S0262176205004517

[45] "LabRATS: Dry Vs. Oil Vacuum Pumps." [Online]. Available: https://sustainability.ucsb.edu/labrats-dry-vs-oil-vacuum-pumps

[46] "Edwards nXDS10i Dry Scroll Vacuum Pump; 7.5 CFM." [Online]. Available: https://www.coleparmer.co.uk/i/edwards-nxds10i-dry-scroll-vacuum-pump-7-5-cfm/7930124?PubID=UY&persist=true&ip=no

[47] "Vacuubrand VACUU·PURE® 10 Screw Pump, US Plug." [Online]. Available: https://www.coleparmer.co.uk/i/vacuubrand-vacuu-pure-10-screw-pump-us-plug/7910408?PubID=UY&persist=true&ip=no

[48] H. Rottländer, W. Umrath, and G. Voss, "Fundamentals of leak detection," 2016. [Online]. Available: https://www.leyboldproducts.com/media/pdf/90/c7/87/Fundamentals_of_Leak_Detection_EN.pdf

[49] D. Tudor and M. Paolone, "Operational-driven optimal-design of a hyperloop system," *Transportation Engineering*, vol. 5, p. 100079, Sep. 2021. [Online]. Available: https://linkinghub.elsevier.com/retrieve/pii/S2666691X2100035X

[50] Dimitrios Kolymbas, *Tunnelling and Tunnel Mechanics A Rational Approach to Tunnelling*. Springer Berlin, Heidelberg, Jul. 2005.

[51] Hyungmin Kang, Yingmei Jin, Hyeokbin Kwon, and Kyuhong Kim, "A Study on the Aerodynamic Drag of Transonic Vehicle in Evacuated Tube Using Computational Fluid Dynamics," *International Journal of Aeronautical and Space Sciences*, vol. 18, no. 4, pp. 614–622, 2017, publisher: . [Online]. Available: http://www.dbpia.co.kr/journal/articleDetail?nodeId=NODE07291467

[52] K. S. Jang, T. T. G. Le, J. Kim, K.-S. Lee, and J. Ryu, "Effects of compressible flow phenomena on aerodynamic characteristics in Hyperloop system," *Aerospace Science and Technology*, vol. 117, p. 106970, Oct. 2021. [Online]. Available: https://www.sciencedirect.com/science/article/pii/S1270963821004806

[53] T.-K. Kim, K.-H. Kim, and H.-B. Kwon, "Aerodynamic characteristics of a tube train," *Journal of Wind Engineering and Industrial Aerodynamics*, vol. 99, no. 12, pp. 1187–1196, Dec. 2011. [Online]. Available: https://www.sciencedirect.com/science/article/pii/S0167610511001723

[54] "Axial-Flow Compressors - an overview | ScienceDirect Topics." [Online]. Available: https://www.sciencedirect.com/topics/engineering/axial-flow-compressors

[55] B. Dodson, "Beyond the hype of Hyperloop: An analysis of Elon Musk's proposed transit system," Aug. 2013. [Online]. Available: https://newatlas.com/hyperloop-musk-analysis/28672/

[56] "Introduction to Air Bearings." [Online]. Available: https://www.specialtycomponents.com/Resources/Technical-Articles/Introduction-to-Air-Bearings/#:~:text=Air%20bearings%20fall%20into%20two,their%20own%20internal%20pressure%20differentials

[57] T. T. G. Le, K. S. Jang, K.-S. Lee, and J. Ryu, "Numerical Investigation of Aerodynamic Drag and Pressure Waves in Hyperloop Systems," *Mathematics*, vol. 8, no. 11, 2020. [Online]. Available: https://www.mdpi.com/2227-7390/8/11/1973

[58] Kenneth Decker, Jeffrey Chin, Andi Peng, Colin Summers, Golda Nguyen, Andrew Oberlander, Gazi Sakib, Nariman Sharifrazi, Christopher Heath, Justin Gray, and Robert Falck, "Conceptual Feasibility Study of the Hyperloop Vehicle for Next-Generation Transport," Feb. 2017. [Online]. Available: https://ntrs.nasa.gov/api/citations/20170001624/downloads/20170001624.pdf

[59] I. A. Hansen, "Hyperloop transport technology assessment and system analysis," *Transportation Planning and Technology*, vol. 43, no. 8, pp. 803–820, Nov. 2020. [Online]. Available: https://www.tandfonline.com/doi/full/10.1080/03081060.2020.1828935

[60] H. Kang, Y. Jin, H. Kwon, and K. Kim, "A study on the aerodynamic drag of transonic vehicle in evacuated tube using computational fluid dynamics," *International Journal of Aeronautical and Space Sciences*, vol. 18, no. 4, pp. 614–622, 2017.

[61] J.-S. Oh, T. Kang, S. Ham, K.-S. Lee, Y.-J. Jang, H.-S. Ryou, and J. Ryu, "Numerical Analysis of Aerodynamic Characteristics of Hyperloop System," *Energies*, vol. 12, no. 3, 2019. [Online]. Available: https://www.mdpi.com/1996-1073/12/3/518

[62] "Aluminium: Specifications, Properties, Classifications and Classes," Apr. 2005. [Online]. Available: https://www.azom.com/article.aspx?ArticleID=2863#:~:text=Pure%20aluminium%20doesn't%20have,properties%20tailored%20to%20particular%20applications.

[63] A. Zhang and Y. Li, "Thermal Conductivity of Aluminum Alloys—A Review," *Materials*, vol. 16, no. 8, p. 2972, Apr. 2023. [Online]. Available: https://www.mdpi.com/1996-1944/16/8/2972

[64] "Properties of aluminium." [Online]. Available: https://www.thyssenkrupp-materials.co.uk/properties-of-aluminium

[65] "UL 94," 2023. [Online]. Available: https://en.wikipedia.org/wiki/UL_94

[66] "TECAPEEK CF30 black." [Online]. Available: https://www.ensingerplastics.com/en-gb/shapes/products/peek-tecapeek-cf30-black#:~:text=Carbon%20filled%20PEEK&text=Its%20carbon%20fibre%20reinforcement%20lends,30%25%20glass%20fibre%20filled%20peek

[67] "Polyether Ether Ketone (PEEK) Recycling." [Online]. Available: https://www.wastetrade.com/resources/plastics/introduction-to-plastics/types-of-plastics/polyether-ether-ketone-peek-recycling/

[68] "Polyaryletherketone (PAEK) Overview." [Online]. Available: https://drakeplastics.com/ultra-high-performance-plastic-materials-solutions-for-your-most-demanding-applications/polyaryletherketone-paek/

[69] "Overview of materials for Polyaryletherketone (PAEK), Glass Fiber Filled." [Online]. Available: https://www.matweb.com/search/datasheet_print.aspx?matguid=48d0107251ef402ebca5e280039cc986

[70] John Grasmeder, "A Closer Peek at PEEK – HPP explained (part 2)," Sep. 2019. [Online]. Available: https://www.victrex.com/en/blog/2017/a-closer-peek-at-peek

[71] "New advanced PAEK products designed for Additive Manufacturing," Jul. 2018. [Online]. Available: https://www.victrexplc.com/news/new-advanced-paek-products-designed-for-additive-manufacturing/

[72] Z. Khan, "BU Research Blog \textbar Forecasting UK Carbon Emissions: The Next 5 to 10 Years \textbar Bournemouth University," Sep. 2023. [Online]. Available: https://blogs.bournemouth.ac.uk/research/2023/09/22/forecasting-uk-carbon-emissions-the-next-5-to-10-years/

[73] Z. Hussain, B. Marcel, A. Majeed, and R. S. M. Tsimisaraka, "Effects of transport–carbon intensity, transportation, and economic complexity on environmental and health expenditures," *Environment, Development and Sustainability*, pp. 1–31, May 2023. [Online]. Available: https://www.ncbi.nlm.nih.gov/pmc/articles/PMC10165593/

[74] G. Santos and O. Smith, "Electric vehicles and the energy generation mix in the UK: 2020–2050," *Energy Reports*, vol. 9, pp. 5612–5627, Dec. 2023. [Online]. Available: https://www.sciencedirect.com/science/article/pii/S2352484723003517

[75] L. Winkler, D. Pearce, J. Nelson, and O. Babacan, "The effect of sustainable mobility transition policies on cumulative urban transport emissions and energy demand," *Nature Communications*, vol. 14, p. 2357, Apr. 2023. [Online]. Available: https://www.ncbi.nlm.nih.gov/pmc/articles/PMC10125996/

[76] "London-Edinburgh rail success proves grounding flights is possible." [Online]. Available: https://environmentjournal.online/transport/london-edinburgh-rail-success-proves-grounding-flights-is-possible/

[77] "London to Edinburgh (Waverley)," publication Title: ScotRail. [Online]. Available: https://www.scotrail.co.uk/train-times/london-to-edinburgh-waverley

[78] "Freight Transportation \textbar MIT Climate Portal." [Online]. Available: https://climate.mit.edu/explainers/freight-transportation

[79] "Transport and environment statistics: 2022," publication Title: GOV.UK. [Online]. Available: https://www.gov.uk/government/statistics/transport-and-environment-statistics-2022

[80] "A Pathway to Net Zero for Road and Rail," publication Title: the University of Bath's research portal. [Online]. Available: https://researchportal.bath.ac.uk/en/projects/a-pathway-to-net-zero-for-road-and-rail

[81] OECD, *The Future of Rail: Opportunities for energy and the environment.* Paris: Organisation for Economic Co-operation and Development, 2019. [Online]. Available: https://www.oecd-ilibrary.org/energy/the-future-of-rail_9789264312821-en

[82] Rafael Mendes Borges and E. Quaglietta, "Assessing Hyperloop Transport Capacity Under Moving-Block and Virtual Coupling Operations," *IEEE Transactions on Intelligent Transportation Systems*, pp. 1–10, Oct. 2021, mAG ID: 3207340901 S2ID: c304aa237142e94f2d78421b539187d780bfba74.

[83] Global Railway Review, "Record passengers travelling between Scotland and London via rail rather than air," Aug. 2017. [Online]. Available: https://www.globalrailwayreview.com/news/61985/record-passengers-travelling-scotland-london-via-rail-rather-air/

[84] Ella Doyle, "More than half of London-Edinburgh travellers are now going by train instead of plane, finds rail expert," *Independent*, Oct. 2022. [Online]. Available: https://www.independent.co.uk/travel/news-and-advice/london-edinburgh-train-rail-lumo-flights-b2205109.html

[85] Gisela Zita Cerron and A. Liem, "THE INTERIOR DESIGN CHALLENGES OF A HYPERLOOP POD HOW TO ENHANCE THE PASSENGER EXPERIENCE," *Proceedings of the Design Society*, 2023, s2ID: d87d5f03caca912bf05815505e9915fa08f887c5.